CARDIFF UNIVERSITY
PRIFYSGOL CAERDYDD

ORCA – Online Research @ Cardiff

This is an Open Access document downloaded from ORCA, Cardiff University's institutional repository:https://orca.cardiff.ac.uk/id/eprint/185648/

This is the author's version of a work that was submitted to / accepted for publication.

Citation for final published version:

Zhu, Hengrui, Wu, Tao, Li, Chun-Feng, Gleeson, Matthew, Wieser, Penny, Lu, Jianggu, Yang, Ming, Scholpp, Jesse L., Heaton, Daniel, Nelson, Wendy, Shervais, John W., Potter, Katherine E., Buchs, David M. , Class, Cornelia, Homrighausen, Stephan, Wang, Xiao-Jun, Kubota, Yusuke, Höfig, Tobias W., Sager, William and Hoernle, Kaj 2026. Unveiling the hotspot-driven magmatic plumbing system of the Center track, Walvis Ridge (South Atlantic Ocean): Insights from mineral geochemistry and isotopic heterogeneity in basalts from IODP Expedition 391. GSA Bulletin 10.1130/b38890.1

Publishers page: https://doi.org/10.1130/b38890.1

Please note:
Changes made as a result of publishing processes such as copy-editing, formatting and page numbers may not be reflected in this version. For the definitive version of this publication, please refer to the published source. You are advised to consult the publisher's version if you wish to cite this paper.

This version is being made available in accordance with publisher policies. See http://orca.cf.ac.uk/policies.html for usage policies. Copyright and moral rights for publications made available in ORCA are retained by the copyright holders.

https://doi.org/10.1130/B38890.1

Unveiling the hotspot-driven magmatic plumbing system of the Center track, Walvis Ridge (South Atlantic Ocean): Insights from mineral geochemistry and isotopic heterogeneity in basalts from IODP Expedition 391

Hengrui Zhu [1], Tao Wu [1, 2 *], Chun-Feng Li [1], Matthew Gleeson [3], Penny Wieser [3], Jianggu Lu [4], Ming Yang [2], Jesse L. Scholpp [5, 6], Daniel Heaton [7], Wendy Nelson [8], John W. Shervais [9], Katherine E. Potter [9], David M. Buchs [10], Cornelia Class [11], Stephan Homrighausen [12], Xiao-Jun Wang [13], Yusuke Kubota [14], Tobias W. Höfig [15], William Sager [16], and Kaj Hoernle [12]

[1]*Ocean College, Zhejiang University, China*
[2]*Hainan Institute of Zhejiang University, China*
[3] *Department of Earth and Planetary Science, University of California, Berkeley, USA*
[4]*Key Laboratory of Submarine Geosciences, Ministry of Natural Resources, China*
[5]*Department of Earth and Planetary Sciences, University of Tennessee, USA*
[6]*Nevada Bureau of Mines and Geology, University of Nevada, USA*
[7]*College of Earth, Ocean, and Atmospheric Sciences, Oregon State University, USA*
[8]*Department of Physics, Astronomy & Geosciences, Towson University, USA*
[9]*Department of Geology, Utah State University, USA*
[10]*School of Earth and Environmental Sciences, Cardiff University, United Kingdom*
[11]*Lamont-Doherty Earth Observatory, Columbia University, USA*
[12]*GEOMAR Helmholtz Centre for Ocean Research Kiel, Germany*
[13]*Department of Geology, Northwest University, China*
[14]*Department of Earth and Planetary Sciences, Japan*
[15]*International Ocean Discovery Program, Texas A&M University, USA*
[16]*Department of Earth and Atmospheric Sciences, University of Houston, USA*

Corresponding author: E-mail addresses taowu@zju.edu.cn (T. Wu)

Abstract

The Tristan-Gough-Walvis Ridge (TGW) volcanic chain on the African plate is one of Earth's longest linear features on the seafloor, however, the origin of its magmatism remains poorly understood. To better understand its formation, temporal

evolution, and geochemical characteristics, six sites were drilled along the TGW chain by International Ocean Discovery Program (IODP) expeditions 391 and 397T: three sites on Valdivia Bank (Site U1575, U1576, and U1577) and three sites in the Guyot Province (Site U1578, Site1584, and U1585). Among these, Site U1578, located on the deep northwestern flank of a "Center track" seamount, represents the deepest basement penetration (>300 m) of both expeditions. According to preliminary geophysical and biostratigraphic constraints, the recovered stratigraphic sections from Site U1578A span >2.0 Myrs during the Paleocene (ca. 62.3-64.8 Ma). Here, we present an integrated study of the mineral major and trace elements, as well as in-situ Sr isotopes of plagioclase (Pl) from Site U1578 basalts. Based on the olivine-spinel (Ol-Sp) thermometry and pyMelt modeling, the calculated mantle potential temperature of the Center track is at least 1400 °C, about 50 °C higher than that of mid-ocean ridge basalts (MORBs), most likely reflecting the influence of a mantle plume. Based on geochemical compositions and crystal textures, we identified three distinct clinopyroxene (Cpx) groups: Group 1 are characterized by high Mg# values (> 83.4), Ni (> 200 ppm) and Cr (> 5000 ppm) contents; Group 2 have intermediate Mg# values (76.6-83.4), Ni (100-200 ppm) and Cr (1000-5000 ppm) contents; Group 3 are characterized by low Mg# values (< 76.6), Ni (< 70 ppm) and Cr (< 30 ppm) contents. Multiple episodes of magma recharge and magma mixing occurred in the plumbing system beneath the Center track, which formed the diversity of mineral textures (i.e., normal zoned, reverse zoned, sector zoned, and oscillatory zoned). Additionally, Pl from this site are isotopically heterogeneous (0.7038±0.0001 to 0.7046±0.0001) and

broadly similar to those of basalts from the northern Tristan track in the Guyot province. A shift to more radiogenic Sr isotopic signatures from the lower to the upper igneous units suggests the increasing incorporation of radiogenic materials into the mantle source, potentially derived from enriched mantle typically associated with basalts on the southern Gough track. These findings indicate that basaltic lavas from the Center track originate from an anomalously hot and geochemically enriched mantle source associated with a mantle plume or hotspot activity. Diverse mineral textures and chemistry record complex fractional crystallization and mixing processes during magma storage prior to eruption.

Keywords: Walvis Ridge; In-situ Sr isotope; Thermobarometer; Crystal zoning; Magmatic plumbing system.

1. Introduction

Most volcanoes on Earth are concentrated at tectonic plate boundaries (i.e., subduction zones and mid-ocean ridges), and their formation can be effectively explained by plate tectonic processes (Palin and Santosh, 2021). However, "intraplate" volcanism can also occur thousands of kilometers away from tectonic plate boundaries (Turcotte et al., 1997). These regions are usually interpreted as the result of mantle melting processes induced by the rising of hot plumes (Campbell and Griffiths, 1990; Campbell and Griffiths, 1992; Duncan and Richards, 1991; Morgan, 1971) or by lithospheric extension (Anderson and Natland, 2014; Hirano et al., 2019). Oceanic

intraplate volcanoes usually have higher crystallization temperatures relative to other tectonic settings (Carter et al., 2024; Jennings et al., 2019; Xu and Liu, 2016; Zhang et al., 2023), and their magma storage depths can vary from very shallow levels (1-5 km) at high-flux volcanoes like Hawaii (DeVitre et al., 2024; Lynn et al., 2024; Wieser et al., 2021), to Moho or uppermost mantle depths in lower-flux systems (Barker et al., 2015; Baxter et al., 2023; Gazel et al., 2025; Gleeson et al., 2025; Gleeson et al., 2020; van Gerve et al., 2024). Additionally, compared to MORBs, intraplate volcanic eruptions are commonly associated with shorter crustal residence times (Bonechi et al., 2024; Petrone et al., 2018) and more rapid magma ascent rates (Klügel et al., 2020; Ma et al., 2024; Peslier et al., 2015), potentially related to their higher volatile contents (Liu et al., 2017) . Thus, investigating the magmatic plumbing system of intraplate volcanoes is essential for understanding their ascent and storage processes prior to eruption, ultimately shedding light on the origins of magmatism.

Mineral phases within volcanic rocks are important recorders of the complex journey of magma transfer through and storage within Earth's mantle and crust (Cashman et al., 2017; Cooper, 2017; Ganne et al., 2018; Neave et al., 2021; Ubide et al., 2021). For example, detailed evaluation of mineral chemistry, chemical zoning and textural features can identify distinct regions of magma storage at depth, mixing between these regions, the processes occurring during magma ascent, and the timescales associated with reservoir destabilization and eruption triggering (Costa et al., 2020; Ginibre et al., 2007; Mutch et al., 2019; Petrone et al., 2022; Streck, 2008). In particular, Pl and Cpx are common in intraplate basaltic magmas, and show chemical

variations correlating with the wide range of pressure-temperature-composition (P-T-X) conditions under which they grow (Bennett et al., 2019; Li et al., 2020; Palummo et al., 2021; Wieser et al., 2024; Zhu et al., 2024). Thus, they are frequently used to decipher complex magma crystallization processes (Chen et al., 2023; Chen et al., 2024; Gleeson et al., 2020; Molendijk et al., 2022; Scholpp et al., 2022; van Gerve et al., 2020; Wei et al., 2022).

Tristan-Gough-Walvis Ridge volcanic chain on the African plate is one of Earth's longest linear features on the seafloor (Sager and Hoernle, 2022), which forms a broad and scattered seamount province leading from the Walvis Ridge to the active volcanic islands of Tristan da Cunha and Gough (Fig.1). It was one of the first seamount tracks proposed to have been formed by a hotspot/mantle plume (Wilson, 1963), a narrow, buoyant, columnar upwelling of higher temperature mantle material driving melting (Morgan, 1971). However, recent research indicates that the hotspot model alone cannot fully explain the complex morphology of Walvis Ridge (Sager et al., 2021). Magnetization models reveal quasi-linear polarity zones that cross the Valdivia Bank and follow predicted paleo-Mid-Atlantic Ridge locations (Thoram et al., 2023), and gravity-derived crustal thickness patterns of Guyot Province are consistent with magmatism emplaced in a spreading-ridge environment (Huang and Li, 2024). These observations provide evidence that, in addition to intraplate hotspot volcanism, magmatic activity linked to mid-ocean ridge processes also contributed to the construction of Walvis Ridge at the same time, implying potential temporal and spatial interactions between plume activity and seafloor spreading. Tristan-Gough-Walvis

Ridge volcanic chain is one of the most studied underwater volcanic chains in the world, and previous studies have mainly focused on whole-rock major-, trace-element geochemistry and Sr-Nd-Pb-Hf isotopic compositions (Class et al., 2015; Hoernle et al., 2015; Homrighausen et al., 2018; Homrighausen et al., 2020; Rohde et al., 2013a; Salters and Sachi-Kocher, 2010), geochronology (Homrighausen et al., 2019; O'Connor and Jokat, 2015a; O'Connor and Jokat, 2015b; Rohde et al., 2013b), and geophysical investigations (Contreras et al., 2022; Geissler et al., 2017; Sager et al., 2021; Thoram et al., 2023; Thoram et al., 2019). Although some studies have explored the magmatic plumbing system of Walvis Ridge (Le Roex, 1985; Weit et al., 2017), their sample collections have been limited to Gough and Tristan da Cunha islands. The Center track, which is located between the Tristan and Gough tracks (Fig.1), is essential for understanding the origin of magmatism in the TGW volcanic chain. Previously, both a triple-zoned plume model and a mixed center zone model have been proposed (Sager and Hoernle, 2022). The mixed center zone model can be further subdivided into two different scenarios: Rohde et al. (2013a, b) proposed that the Gough and Tristan hotspot tracks resulted from a bifurcated plume, whereas Homrighausen et al. (2023) proposed that the two tracks originated from distinct plumelets rising independently from the deep mantle. In this study, we focus on examining these models through the investigation of the Center track.

We examine the in-situ major and trace element compositions of Ol, Sp, Cpx, Pl, and in-situ Sr isotopic compositions of Pl from basalts collected at IODP 391 Site U1578, located in the Center track. We aim to elucidate the complex magmatic

plumbing system and to determine the origin of magmatism in the Center track of Walvis Ridge.

2. Geological setting and samples

According to the mantle plume model (Morgan, 1971; Richards et al., 1989; Wilson, 1973), Walvis Ridge hotspot volcanism started with the emplacement of the Parana-Etendeka continental flood basalt province at ~132 Ma (Renne et al., 1996). From northeast to southwest, TGW volcanic chain contains a ridge (Frio Ridge), an oceanic plateau (Valdivia Bank), and chains of guyots, and scattered seamounts called the Guyot Province (Sager and Hoernle, 2022). The post-70 Ma Guyot Province is divided into three distinct seamount tracks: the Gough track, the Center track, and the Tristan track (Fig.1). Radiogenic isotope ratios reveal spatial zonation in the chemical composition of these post-70 Ma lavas (Class et al., 2015; Hoernle et al., 2015). Previous studies, based on free-air gravity data and the age-distance relationship of volcanism, suggested that Tristan track was influenced by hotspot interaction with the Mid-Atlantic Ridge (O'Connor and Jokat, 2015a), whereas the Center track and Gough track were generated by hotspots beneath the African plate. However, the mechanism and details of plume-ridge interaction and plume-lithosphere interaction processes are not well understood.

To better understand the formation and evolution of Walvis Ridge, IODP Expedition 391 drilled four sites (Sites U1575 to U1578) during December 2021 to February 2022. Site U1578, the focus of this study, is located on the deep northwestern

flank of Center track, where Walvis Ridge splits (red circle in Fig.1). Igneous rocks were recovered from Site U1578, representing the deepest basement penetration established during Expedition 391 at 302.14 m. The igneous units comprise pillow and lobate flows, sheet flows, and massive flows with interbedded calcareous sedimentary rocks and volcaniclastic deposits (Fig.2). According to the preliminary geophysical and biostratigraphic studies reported in the expedition report (Sager and Hoernle, 2022), a geologic time span of >2.0 Myrs during the Paleocene (ca. 62.3-64.8Ma) was recovered from Site U1578A. In addition, we observe significant differences in mineral geochemistry between the early and late stages (see Discussion below) and therefore subdivide the Site U1578 samples into upper (Section 20R-30R) and lower units (Section 31R-65R; Fig.2). This subdivision is consistent with the lithostratigraphic division reported in the IODP expedition report (Sager and Hoernle, 2022). The basaltic samples from Site U1578 show a porphyritic texture and contain phenocrysts of Pl, Cpx and Ol. The groundmass often contains Pl, Cpx, skeletal Fe oxide crystals, and Ol. Plagioclase phenocrysts (~10 vol% and 0.5-5 mm) usually exhibit oscillatory zoning (Figs.3a, b). In some samples, Pl phenocrysts show patchy zoning, which consists of irregular corroded cores (Fig.3c). Clinopyroxene phenocrysts (~5 vol% and 0.5-2 mm) also commonly display zoning textures (i.e., core-mantle-rim) and some of them exhibit internal resorption textures (Figs.3d-3f). Note that we use the term “mantle” to refer to the optically distinguishable area between core and rim for zoned Cpx. Most of the Ol phenocrysts (< 5 vol% and 0.5-2 mm) are euhedral to subhedral and usually have Sp and melt inclusions (Figs.3g-3i). Olivine and spinel in this study do not show significant

zoning textures. Olivine-hosted Sp crystals range in size from 5μm to 20 μm. Fe oxide crystals in the groundmass appear to be titanomagnetite and ilmenite based on their crystal habit and optical appearance under transmitted and reflected light.

3. Analytical methods

3.1 Whole-rock major elements

Whole-rock major elements were conducted at the Key Laboratory of Submarine Geoscience, Second Institute of Oceanography (Hangzhou, China). The sample pretreatment of whole rock major element analysis was made by the fusion bead method (Johnson et al., 1999). The flux, which was used for the sample fusion, is a mixture of lithium tetraborate, lithium metaborate, and lithium fluoride (45:10:5), Ammonium nitrate and lithium bromide were used as oxidant and release agents respectively. The melting temperature was 1050 ℃ and the melting time was 15 minutes. A Zsx Primus II wavelength dispersive X-ray fluorescence spectrometer (XRF) produced by RIGAKU, Japan, was utilized for the analysis of the major elements in the fused pellets. The X-ray tube used in the analysis was equipped with a 4.0-kW end-window Rh target. In this study, the Chinese National standards (GBW07103, GBW07104, GBW07105, GBW07310, GBW07312, GBW07314, and GBW07316) were used to monitor the data quality. The relative standard deviations are within ±5% and all the results are listed in Table S1A.

3.2 Mineral major- and trace-elements

We performed 404 in-situ major and trace element measurements of Ol and Sp crystals extracted from 4 core sections. The composition of Ol and Sp was determined using an Oxford Instruments Ultim Max energy dispersive spectrometry (EDS) detector and an Oxford Instruments Wave wavelength dispersive spectrometry (WDS) detector on the JEOL JSM IT800HL FEG-SEM in the Earth and Planetary Science Department at UC Berkeley. The JEOL FEG-SEM provides a large range of possible beam conditions which can be measured with an in-column Faraday cup, providing access to higher beam currents (~150 nA) suitable for minor-element analysis by WDS and lower beam currents for EDS (~2 nA). For EDS analyses, nepheline (Si), Fe_metal (Fe), diopside (Ca, Mg), MnO (Mn), NiO (Ni), Al_2O_3 (Al), TiO_2 (Ti), and Cr_2O_3 (Cr) were used as calibration standards. Olivine (from Microanalysis Consultants), San Carlos, Mong-Ol, and Chromitite were used to monitor the accuracy of the measurements as well as analytical drift (see Table S1B for full list of standard sources). During EDS analyses, the beam was rastered over a 1-1.5 μm area using a beam current of 2 nA and an accelerating voltage of 20 kV to determine the FeO-MgO-SiO_2-CaO-MnO-NiO in Ol and FeO-MgO-SiO_2-TiO_2-Al_2O_3-Cr_2O_3 in Sp crystals. Following EDS analyses, the beam current was increased to 150 nA and the aluminum (Al) content in Ol, at the location of each EDS analysis, was determined via WDS. Counts of Al were collected for 90 seconds on peak, and background counts were collected for 45 seconds on either side of the peak. The WDS Al measurements were calibrated on an Al_2O_3 standard. Under these conditions, the analytical uncertainty (1σ) for Al in Ol was ~17 ppm. A profile of points spaced 2-3 μm apart was collected for each Ol-Sp pair, see Table S1B

for more information.

In total, we performed 120 in-situ major element measurements of Pl crystals extracted from 11 core sections and 553 measurements of Cpx crystals extracted from 15 core sections at Site U1578 (Fig.2). All the results are listed in Tables S1C and D. The chemical compositions of these crystals were measured on polished thin sections by a four-spectrometer Jeol JXA 8100 electron probe microanalyzer (EPMA) in the Key Laboratory of Submarine Geoscience, State Oceanic Administration, Second Institute of Oceanography (Hangzhou, China). Back-scattered electron images were utilized to check the homogeneity of the phenocrysts and the crystal zoning. We used an accelerating potential of 15 kV, a beam current of 20 nA, and a spot size of 5 μm for most analyses. Smaller crystals were analyzed using a 1-3 μm spot. Jadeite (Na), olivine (Mg), hematite (Fe), pyrope garnet (Al), diopside (Si and Ca), orthoclase (K), fluorapatite (P), rutile (Ti), nickel oxide (Ni), and rhodochrosite (Mn) were used for calibration standards (Tables S1C). Element peaks and backgrounds were measured for all elements with counting times of 10 s and 5 s, respectively (except for Fe, and Mn, which were 30 s and 15 s, respectively). Each sample was analyzed 10 times in different locations, and the precision (1σ) is < 3% for Si, Al, Fe, Mg, Ca, and 8% for Ti, and Na based on repeated standard and sample analyses.

A total of 42 Cpx grains from 6 core sections were selected for trace element analysis in this study and all the results, including standard samples, are shown in Table S1E. Trace element analysis of Cpx was conducted at the laser ablation-induced coupled plasma-mass spectrometry (LA-ICP-MS) laboratory in the School of Earth

Science, Zhejiang University, China. Analyses were performed using an iCAP-RQ single-collector quadrupole ICP-MS (Thermo Fisher Scientific, Waltham, USA) coupled to an Analyte G2 ArF excimer laser ablation (LA) system equipped with HelEx 2 volume sample chamber (Teledyne Cetac Technologies, Omaha, USA). The spot size and frequency of the laser were set to 60 μm and 5 Hz respectively, and all laser analyses were targeted at the cores of individual Cpx grains rather than their rims. The fluency of the laser analyses was 18 J/cm^2. Each analysis incorporated a background acquisition of approximately 20-30 s followed by 50 s of data acquisition from the sample. Two geochemically distinct reference glasses (BCR-2G, BHVO-2G) were used to cover the possible geochemical spectrum. Every 6 sample analyses were followed by two analyses of NIST SRM 610 to correct the time-dependent drift of sensitivity and mass discrimination. We employed a multi-external-standard without internal-standard approach, processing our data using the ICPMSDataCal software (Liu et al., 2008). The software was used to perform off-line selection and integration of background and analytic signals, as well as time-drift correction and quantitative calibration for trace element analysis. Relative standard deviations (% RSD) of LA-ICP-MS analyses are less than 10% for all trace elements.

3.3 In-situ Sr isotopes of Pl

In-situ Sr isotope analyses of Pl were performed on a Neptune Plus MC-ICP-MS (Thermo Fisher Scientific, USA) coupled with Geolas Pro 193 nm ArF excimer laser ablation system (Coherent, Gottingen, Germany) at State Key Laboratory of

Lithospheric Evolution (SKLLE), Institute of the Geology and Geophysics, Chinese Academy of Sciences (IGGCAS). Detailed operating conditions for the laser ablation system and the ICP-MS instrument and data reduction are the same as described by Xu et al. (2022). During the LA-MC-ICP-MS analysis, the laser had an energy density of 2.8 J/cm^2, a frequency of 8 Hz, and a beam spot size of 130 μm. Two natural Pl standards, BDL and JH-56 were used as unknown samples to verify the accuracy of the calibration method for in situ Sr isotope analyses. The measured values of BDL and JH-56 are consistent with the recommended values (Xu et al., 2022; Yang et al., 2009) and all the results are listed in Table S1F.

4. Results

4.1 Whole-rock major elements

We present major element data for eight Center track volcanic rock samples from different core sections of Site U1578 (Fig.2; Table S1A) and all major elements have been recalculated to 100 wt.% on a volatile free basis for further discussion. All volcanic rocks are characterized by relatively high total alkali contents ($Na_2O + K_2O$ = 3.7-5.5 wt.%) and plot mainly within the field of alkaline basalt and trachybasalt in the TAS classification diagram (Fig.4). U1578 volcanic rocks have relatively low Mg# values (39.2-53.0; Mg# = 100×Mg/(Mg + Fe_{tot}), where Mg and Fe_{tot} represent molar proportions) and low MgO contents (4.4-7.8 wt.%; Table S1A), indicating relatively evolved magmas. Comparisons to the published geochemical data (Class and le Roex, 2008; Cliff et al., 1991; EWART et al., 2004; Gibson et al., 2005; Hoernle et al., 2015;

296 Homrighausen et al., 2019; Homrighausen et al., 2023; Le Roex, 1985; Le Roex et al.,
297 1990; Rohde et al., 2013a; Salters and Sachi-Kocher, 2010; Willbold and Stracke, 2006;
298 Willbold and Stracke, 2010) indicate that U1578 volcanic rocks plot within the Gough
299 track (including Gough Island) field in the TAS classification diagram (Fig.4). Most
300 volcanic rocks from the Tristan track (including Tristan Island) have higher total alkali
301 contents and lower SiO_2 contents, belonging to tephrite basanite series.
302
303 4.2 Major and minor-elements of Ol and their Sp inclusions
304 Olivine phenocrysts and their Sp inclusions are common in some Site U1578
305 basalts (Fig.2). Olivines from upper igneous units (i.e., Section 28R) display higher Fo
306 values (87.8-90.5; Fo = 100×Mg/(Mg + Fe_{tot}), where Mg and Fe_{tot} represent molar
307 proportions) and MgO contents (46.49-49.10 wt.%), whereas Ols from lower igneous
308 units (i.e., Section 53 and 60R) have lower Fo values (79.9-88.6) and MgO contents
309 (41.86-48.74 wt.%). Olivines show negative correlations between CaO, MnO, and Fo
310 values, and positive correlations between NiO, and Fo values, and no clear correlation
311 between Al_2O_3 and Fo (Fig.5). Olivines in U1578 volcanic rocks record variations in
312 NiO and MnO concentrations between 0.18-0.44 wt.% and 0.10-0.30 wt.% respectively,
313 and CaO contents range from 0.22-0.45 wt.% (Table S1B). We suggest that these Ol
314 phenocrysts are not mantle-derived xenocrysts because of their significantly higher
315 CaO and MnO contents relative to those of Ol in mantle xenoliths (Ren et al., 2004;
316 Thompson and Gibson, 2000). The Ol-hosted Sp inclusions from U1578 are Cr-rich
317 and exhibit Cr# of 38.4-67.7 (Cr# = 100×Cr / (Cr + Al), where Cr and Al represent

molar proportions). Al_2O_3 (15.53-33.10 wt.%) and Cr_2O_3 (27.53-48.55 wt.%) contents of the Sp crystals in studied samples plot along the Cr-Al trend (Barnes and Roeder, 2001), which Irvine (1967) explained as lines corresponding to Sp equilibrating with Ol of constant composition at constant temperature. Notably, Sp inclusions from upper igneous units usually have higher Cr# values (60.8-67.7, average = 65.99) and lower Al_2O_3 contents (15.53-17.69 wt.%, average = 16.15) than those from lower igneous units (Fig.6b; Table 1). Also, Sp inclusions from upper igneous units plot within the ocean island basalt (OIB) field in the diagram of TiO_2 versus Al_2O_3 (Kamenetsky et al., 2001), which is consistent with the geological setting of Site U1578 (Sager and Hoernle, 2022). However, Sp inclusions from lower units plot in the transitional field between OIB and MORB, and even within the MORB field (discussed below). Regarding the OIB field in Fig.6b, it is defined based on multiple OIB localities, including Hawaii (Kilauea, Mauna Loa, Mauna Kea), Reunion, and French Polynesia (Tubuai, Mangaia).

4.3 Major, trace-elements of Cpx

Clinopyroxene crystals from Site U1578 have compositions spanning $Wo_{38-48}En_{28-49}Fs_{7-25}$ (Wo = 100×Ca/(Mg + Fe + Ca); En = 100×Mg/(Mg + Fe + Ca); Fs = 100×Fe/(Mg + Fe + Ca)) and mainly classified as diopside and Ca-rich augite (Fig.7a; (Morimoto et al., 1988). Complex variations in Cpx chemistry are observed between different samples, but there is no obvious correlation between the depths of Site U1578 and Cpx compositions (Table S1C). Clinopyroxenes from Site U1578 display positive correlations between CaO and Mg# values, negative correlations between TiO_2, FeO_t,

MnO, Na_2O, and Mg#, and no correlation between Al_2O_3 and Mg# (Fig.S1). In this study, we use macrocrysts and microlites to refer to crystals larger than 200 μm and smaller than 200 μm, respectively. Clinopyroxene macrocrysts usually have higher CaO (20.01-21.86 wt.%), Mg# values (74.4-88.0) and lower Na_2O (0.24-0.49 wt.%), FeO_t (4.01-9.18 wt.%), and TiO_2 (0.81-1.89 wt.%) contents than those of Cpx microlites (CaO = 18.06-21.14 wt.%; Mg# = 53.2-79.7; Na_2O = 0.23-0.55 wt.%; FeO_t = 7.01-13.91 wt.%; TiO_2 = 0.91-3.58 wt.%; Table S1C). Clinopyroxene macrocrysts from Site U1578 usually display significant zoning textures (Fig.3) and complex geochemical variations (Fig.S1). The compositional zoning of Cpx macrocrysts could reflect sequential changes in the magmatic environment through time (Ubide et al., 2021) or the recycling of antecrysts in the plumbing system (Molendijk et al., 2022).

The abundance of Ni and Cr in all Cpx crystals are positively correlated with Mg# values, whereas V, Co, Zn, and Zr are negatively correlated with Mg# values (Fig.8; Table S1E). No correlation exists between Sc, Sr, and Mg# values. The chondrite-normalized patterns (Sun and McDonough, 1989) of rare earth elements (REE) in Cpx exhibit sub-parallel trends and convex-upward REE patterns (Fig.9a). Clinopyroxene microlites exhibit higher REE contents and more pronounced negative Eu anomalies ($Eu/Eu^* = Eu_N/ (Sm_N \times Gd_N)^{0.5}$; 0.72-0.89) than Cpx macrocrysts (0.84-1.12; Fig.8f), indicating the abundant crystallization of Pl in the groundmass during late stage melt differentiation (Palummo et al., 2021). In the primitive mantle (PM)-normalized multi-element spectra (McDonough and Sun, 1995), Cpx crystals show negative Ba, Nb, and Sr anomalies (i.e., Sr/Nd_{PM} = 0.07-0.56), positive Th anomaly (i.e., Th/Ba_{PM} = 4.67-

147.42) and depletion of Zr and Hf relative to the neighboring elements (i.e., Zr/Sm_{PM} = 0.30-0.55, Hf/Sm_{PM} = 0.43-0.94; Fig.9b). Using the experimentally measured partition coefficients of REE between coexisting Cpx and melt (Sun and Liang, 2012), we calculate the REE patterns of the parental melts in equilibrium with Cpx (Fig.9a), which closely resemble the average whole-rock OIB composition from Sun and McDonough (1989).

4.4 Major elements and in-situ Sr isotopic compositions of Pl

Plagioclase crystals collected from different units of Site U1578 were analyzed for major elements using EPMA (Fig.2; Table S1D). Plagioclase macrocrysts are mainly bytownites with compositions of $Ab_{13.7-35.0}An_{63.6-85.8}Or_{0.4-1.5}$ (Ab = 100×Na/(K + Na + Ca); An = 100×Ca/(K + Na + Ca); Or = 100×K/(K + Na + Ca)), whereas Pl microlites are labradorites with compositions of $Ab_{28.8-41.8}An_{56.3-70.1}Or_{1.0-1.9}$ (Fig.7b). Some Pl macrocrysts display normal zoning textures (Fig.3b) with decreasing An values from core to rim (Fig.7c). Negative correlations between An and TiO_2 and FeO are clearly observed (Fig.S2). Ninety in-situ Sr isotopic analyses have been conducted for 16 Pl macrocrysts from Site U1578 (Table S1F), displaying significant variations in $^{87}Sr/^{86}Sr$ isotopes (0.7038 ± 0.0001 to 0.7046 ± 0.0001). It is important to note that abrupt changes in the $^{87}Sr/^{86}Sr$ isotope composition between upper igneous units (0.7044 ± 0.0001) and lower igneous units (0.7040 ± 0.0001) are observed (Table 1). All reported $^{87}Sr/^{86}Sr$ values are presented with ±2σ analytical uncertainty

5. Discussion

5.1 Evidence for the thermal anomaly of Center track

Temperature is a fundamental property of magmas and can be used to identify their origin and tectonic setting (Herzberg, 2011; Herzberg and Asimow, 2008; Putirka, 2005; Zhang et al., 2023). In this study, the Al-in-Ol thermometer from Zhang et al. (2023) is applied to calculate the crystallization temperature of Ol. This thermometer is not affected by crystallization pressure, melt composition, oxygen fugacity, and water content (Coogan et al., 2014; Wan et al., 2008). Details of the Al-in-Ol thermometer method and Monte Carlo error propagation approach used to assess the impact of analytical uncertainty are included in the Supplementary Text S1 and Table S2. Crystallization temperatures calculated from Ol-Sp pairs in U1578 samples show a large range, with an expected increase in temperature with increasing Fo content (1205.6 ± 23.9 ℃ to 1288.5 ± 23.9 ℃; 1SE; Fig.10a). At a given Fo content, Ol in this study exhibits significantly higher crystallization temperatures than those of global MORBs (Coogan et al., 2014; Matthews et al., 2021), but similar to those estimated from Iceland (Matthews et al., 2016; Spice et al., 2016). This observation supports the presence of anomalously hot primary melts and indicates a thermal anomaly in the mantle source beneath the Center track.

To further constrain the thermal anomaly in Center track of Walvis Ridge, we calculated mantle potential temperatures (Tp) using pyMelt modeling. PyMelt is an open-source python library for calculating the melting behavior of the Earth's mantle (Matthews et al., 2022). As a forward modeling tool, pyMelt allows users to input

406 mantle potential temperature and mantle source lithology proportions to estimate the
407 primary crystallization temperature. Therefore, to estimate the mantle potential
408 temperature, we need to constrain both the approximate proportion of pyroxenite in the
409 mantle source beneath the Center track and the primary crystallization temperature of
410 the magmas. For the mantle source lithology, two melting lithologies (the KLB-1
411 lherzolite (Katz et al., 2003), and the silica-undersaturated pyroxenite KG1 (Kogiso et
412 al., 1998)) are used. We set four possible source pyroxenite fractions (px = 10%, 15%,
413 20%, and 25%) based on a previous study from Gough and Tristan da Cunha Island (Li
414 et al., 2025). For the primary crystallization temperature, we extrapolate a liquid line of
415 descent from the Ol-Sp crystallization temperature to Fo = 91 (following the method
416 from Matthews et al. (2021)), which would be in equilibrium with a lherzolitic mantle
417 source. This yields a maximum primary magma temperature of 1401°C for the lower
418 unit and 1316 °C for the upper unit (Fig.10a). For each lithology condition, we tested
419 13 different mantle potential temperatures in pyMelt and then used linear interpolation
420 to determine the Tp values required to produce the primary magmatic temperatures
421 calculated above (red dashed lines in Fig.10b). The pressure at which melting
422 terminated (representing lithospheric pressure) was set to 1.5 GPa, based on data from
423 Tristan da Cunha Island (Li et al., 2025), and the crystallization pressure was set to 0.4
424 GPa based on constraints from Cpx barometry (Supplementary Text S2). The
425 uncertainties on Tp were estimated by propagating the errors from the Ol thermometer
426 and from extrapolating the liquid line of descent used to calculate the primary
427 crystallization temperature. The results show that the Tp required to recreate the

crystallization temperature of the lower unit ranges from 1522 °C (px = 10%) to 1580 °C (px = 25%). It should be noted that these calculated Tp values of the lower unit are ~200 °C higher than those of ambient MORB-source mantle (typically ~1350 °C). However, these estimates should be regarded as absolute upper limits of Tp, and the actual values may be significantly lower. Several factors could lead to overestimation, including: (i) a high contribution of pyroxenite-derived melts, which would invalidate the assumption that the primary mantle melts are in equilibrium with Fo_{91} Ol as the most primitive Ol in such melts would likely have a lower Fo content (Li et al., 2025); and (ii) the abundant crystallization of phases other than Ol (e.g., Cpx and Pl), which would change the crystallization path and reduce the applicability of the Ol-based reverse crystallization method from Matthews et al. (2021). Interestingly, the upper unit yields Tp estimates of 1373°C (px = 15%) to 1424 °C (px = 25%), significantly lower than the lower unit. We consider these upper unit values, derived from an Ol with Fo > 90, to be representative of the lower bound of possible mantle potential temperature beneath the Center track (~1400 °C). The difference in Tp between the upper and lower units may reflect variations in the proportion of pyroxenite in the mantle source and/or the spatial variation within the plume itself. Considering relative plate motion, the higher Tp of the lower units may correspond to the center of the plume, whereas the lower Tp of the upper units – which are believed to be 2 Myrs younger (Sager and Hoernle, 2022) – may correspond to the plume edge, an issue that requires further investigation in future work.

Taken together, our results suggest that the Center track of Walvis Ridge is derived

from a source that is at least 50 °C hotter than the mantle sources beneath mid-ocean ridge settings (Fig.10c). This indicates that a hotspot or mantle plume may have fed this track. The REE patterns of the parental melts in equilibrium with Cpx are elevated in LREE relative to HREE in a manner that is more similar to published OIB than MORB data (Sun and McDonough, 1989), which is also consistent with a hotspot or mantle plume origin (Hofmann and White, 1982). A plume origin is also supported by identification of enriched mantle one (EMI) components in the source region of the Tristan-Gough-Walvis Ridge hotspot track (Hoernle et al., 2015; Homrighausen et al., 2020; Homrighausen et al., 2023) and a rising plumelet just southwest of the Tristan island group based on the local seismic tomography (Schlömer et al., 2017). The elevated $^{3}He/^{4}He$ isotope signatures in the basalts from both upper and lower units of U1578 (17.48±1.45 R_A; Scholpp et al., 2025) indicate that the presence of a primordial, undegassed mantle component in the mantle source region beneath the Center track - most likely originating from lower-mantle material entrained into an upwelling plume structure (Homrighausen et al., 2019; Homrighausen et al., 2020; Homrighausen et al., 2023). Combined with the preliminary age of Site U1578 (62-64 Ma) (Sager and Hoernle, 2022), we propose that the mantle plume beneath the Center track of Walvis Ridge was active and carried heat upward in rising columns of hot material at 62-64 Ma. This helps to explain why the magma production rate of Guyot Province was relatively high at 62-64 Ma (Huang and Li, 2024). In summary, our new data indicates that there was a thermal anomaly in the source region of the Center track, which was most likely related to a mantle plume.

472

473 5.2 Characteristics and origins of the diversity of crystal zonings

474 Mineral textures and associated in-situ compositional variations can record
475 information about crystallization conditions at the scale of an entire magmatic plumbing
476 system and provide crucial information about magma transfer and storage through
477 Earth's mantle and crust (Giacomoni et al., 2016; Li et al., 2020; Nardini et al., 2024;
478 Palummo et al., 2021; Pelullo et al., 2022; Wei et al., 2022; Zhang et al., 2024). In this
479 study, we conduct a K-means cluster analysis on N=42 crystals using eight geochemical
480 parameters of Cpx; Mg#, Na_2O, Sc, Cr, Ni, La, Y and jadeite (Jd) content from LA-
481 ICP-MS data. K-means clustering was performed in Python using the scikit-learn
482 package (Pedregosa et al., 2011). Data were first standardized using StandardScaler,
483 before applying KMeans to classify all crystals into three groups and principal
484 component analysis (PCA) was applied to visualize the clustering results (Fig.S5). Mg#,
485 Sc, Cr, and Ni are sensitive to melt composition and fractionation degree, while La and
486 Y capture the variability in trace element enrichment and depletion of the mantle source.
487 Na_2O and Jd content are included because they are more sensitive to crystallization
488 pressure and temperature (Putirka et al., 2003). Together, these parameters provide a
489 good balance between major and trace element information.

490 The average major and trace element compositions of Cpx from Groups 1-3 are
491 summarized in Table 2, with detailed data available in Tables S1C and S1E. Group 1
492 are characterized by high Mg# values (> 83.4), Ni (> 200 ppm) and Cr (> 5000 ppm);
493 Group 2 have Mg# values of 76.6- 83.4, Ni and Cr contents of 100-200 ppm and 1000-

494 5000 ppm; and Group 3 are characterized by low Mg# values (< 76.6), Ni (< 70 ppm)
495 and Cr (< 30 ppm) contents. The distinct Mg# of these groups was used to classify the
496 N=553 EPMA analyses, given the lack of high-quality trace element data for these spots
497 to perform the full clustering. 21% of these EPMA analyses are classified as Group 1,
498 49% as Group 2 and 30% as Group 3. There is sufficient range in the Mg# of individual
499 crystals that different zones within the same crystal can be linked to different groups
500 (i.e., Group 1-3 in Fig.11a, Group 2-3 in Fig.11b). We calculate the crystallization
501 temperatures and pressures of Cpx using Cpx-melt and Cpx-only thermobarometry (see
502 Supplementary Text S2 for details), and the results are presented in Table S3.

503 When considering zoning across the crystal, pyroxenes show four textural types:
504 (1) euhedral, unzoned crystals; (2) normally zoned crystals with higher Mg#, Cr_2O_3,
505 and CaO, and lower Na_2O, TiO_2, FeO, and MnO contents in their cores/mantles
506 compared to their rims (i.e., Fig.3d); (3) reverse-zoned crystals with intermediate
507 compositions in their cores and higher Mg# values in their mantles or rims (i.e., Fig.3e);
508 and (4) sector-zoned crystals (i.e., Fig.3f). In this study, sector zoning in Cpx consists
509 of Si-Mg-rich, Al-Ti-poor hourglass forms {-1 1 1} and Si-Mg-poor, Al-Ti-rich prism
510 forms {h k 0} (Table S1). In addition, sector zoning in Cpx at Site U1578 follows typical
511 sector partitioning in alkaline magma systems (Downes, 1974; Kouchi et al., 1983;
512 Leung, 1974; Mollo et al., 2020; Ubide et al., 2019), suggesting low degrees of
513 undercooling in a dynamic crystallization regime (Di Stefano et al., 2020; Klügel et al.,
514 2020; Masotta et al., 2020; Tapu et al., 2022). However, the absence of sector zoning
515 in most Cpx phenocrysts suggests crystallization under even lower degrees of

516 undercooling during slower magma ascent, where growth rates were reduced to
517 approach near-equilibrium conditions (Ubide et al., 2019).

518 Within each of these zoned crystals, individual points making up transects can be
519 classified into Group 1-3 using the clustering algorithm. Some normally zoned crystals
520 show a core with high Mg# (> 83.4; Group 1), a mantle with intermediate composition
521 (Mg# = 76.6-83.4; Group 2) and a rim with low Mg# (< 76.6; Group 3; Fig.11a). Within
522 the three zones, the composition is relatively constant, with sharp transitions between
523 zones. Other crystals have an intermediate core (Mg# = 76.6-83.4; Group 2) and a rim
524 characterized by low Mg# (< 76.6; Group 3), and the width of this rim can differ
525 (Figs.11b, 11c). Some reversely zoned crystals have intermediate Group 2 cores, with
526 a mantle of more primitive Group 1 compositions, before dropping back to more
527 evolved Group 2 compositions with a continuous drop in Mg# towards the rim (Fig.
528 11d). Others have very evolved Group 3 cores, passing into more primitive Group 2
529 mantles, and finally dropping in Mg# towards the rim (Fig.11e). In summary, Cpx
530 crystals at Site U1578 show various zoning patterns and sharp geochemical
531 composition changes from their cores, and mantles to their rims, suggesting these Cpx
532 crystals have undergone complex crystallization processes within different magmatic
533 environments marked by the plateaus of relatively constant composition (Ginibre et al.,
534 2007; Jerram and Martin, 2008; Streck, 2008; Ubide et al., 2021).

535 According to the similar trace element patterns (Fig.9) and continuous variation
536 trends on the plots of trace element (i.e., Cr, Ni, and V) against Mg# (Fig.8), we suggest
537 that the three different Cpx groups (Group 1, Group 2 and Group 3) in the Center track

538 of Walvis Ridge crystallized from co-genetic magmas (Jankovics et al., 2016; Li et al.,
539 2020; Liu et al., 2022; Wei et al., 2022; Zhang et al., 2024). Based on the distinct core
540 compositions of Cpx from Group 1, Group 2, and Group 3 (Fig.11), we propose that
541 three different magmatic environments (MEs) existed beneath the Center track, named
542 ME1, ME2, and ME3, respectively. The high Mg# Group 1 cores of normally zoned
543 Cpx (i.e., Fig.11a) are interpreted to crystallize in a more primitive magmatic
544 environment (ME1), which is consistent with their higher Cr (> 5000 ppm) and Ni (>
545 200 ppm) contents (Fig.8). Subsequently, they were incorporated into more evolved
546 magmas where they grew low Mg# mantles and rims (i.e., ME2). Normally zoned Cpx
547 with intermediate Group 2 cores (i.e., Figs.11b, 11c) are interpreted to crystallize in a
548 more evolved magmatic environment (ME2) than crystals with Group 1 cores. The
549 relatively sharp compositional changes between different zones indicates rapid
550 transition to a new set of conditions stabilizing a different Cpx composition, here
551 inferred to represent a new magmatic environment. The rims of the normally zoned Cpx
552 shown in Fig.11c are relatively thin (<20 μm) compared to the thicker (~75 μm) rims
553 of the Cpx shown in Fig.11b. Based on the Fe-Mg interdiffusion rates in Cpx (Müller
554 et al., 2013), the thin rims of Cpx in Fig.11c and the lack of a compositional plateau
555 indicate that they likely formed during ascent, cooling and crystallization of the
556 groundmass, rather than prolonged storage in ME3 (Dimanov and Wiedenbeck, 2006;
557 Mollo et al., 2010; Zhang et al., 2024). On the contrary, the plateau in Mg#, CaO and
558 TiO_2 for the Group 3 rim in Fig.11b is more consistent with crystallization from a cooler,
559 evolved melt in a relatively stable environment (ME3) (Cao et al., 2022; Ma et al.,

2024).

Reverse-zoned Cpx is generally related to magma mixing, suggesting an open system behavior of the magmatic system (Ginibre et al., 2007; Liu et al., 2022; Molendijk et al., 2022; Streck, 2008). In BSE photomicrographs of reverse-zoned Cpx shown in Fig.11d, a subhedral light grey crystal core (Group 2) is surrounded by a dark grey mantle with higher contents of Mg# and Cr_2O_3 and lower contents of TiO_2 and FeO (Group 1). We suggest that the internal patchy shape reflects thermal erosion as a consequence of hot, mafic magma input from ME1 into the resident evolved crustal magma reservoir (Ma et al., 2024; Palummo et al., 2021), which was followed by crystallization forming the more euhedral darker rim. Reverse-zoned Cpx with highly evolved Group 3 cores (Fig.11e) crystallized in the most evolved magmatic environment (ME3), before the injection of more mafic magma from ME2 that partially dissolved the pre-existing crystal core during the evolved stage. This further suggests that magma mixing was relatively common within ME3. It should be noted that, although the cores of reverse-zoned Cpx shown in Fig.11e and the rims of some normally zoned Cpx (i.e., Fig.11b) are all classified as Group 3 based on Mg# alone, they are chemically distinct. The composition of cores showing Group 3 characteristics have a very small range of Mg# values (72.5-76.6). In contrast, the rim analyses classified as Group 3 have a much wider range of Mg# values (62.5-76.6), and extend up to far higher TiO_2 and Al_2O_3 contents (Fig.S9). We interpret the cores to have formed in the relatively stable ME3 with a relatively narrow range of compositions, and the rims to have formed during additional crystallization during ascent and syn-eruptive

582 quenching at the seafloor (Giacomoni et al., 2021; Giacomoni et al., 2016; Streck, 2008).

583 The complex magma recharge and mixing processes revealed by Cpx are also
584 supported by the chemical zoning in Pl phenocrysts (Fig.S10). Plagioclase phenocrysts
585 from Site U1578 are usually oscillatory zoned and can be divided into fine banding and
586 coarse banding based on the width of the zoning (Cao et al., 2022; Downes, 1974;
587 Streck, 2008). The widths of oscillatory coarse banding in Site1578 Pl lie typically
588 above 50 μm and can exceed 200 μm in some cases (i.e., Figs.S10a, S10d), which
589 usually results from magma mixing (Streck, 2008; Yang et al., 2019) or polybaric-
590 isothermal convection in a large magma chamber (Ustunisik et al., 2014). While the
591 latter mechanism is possible given that experimental data indicates a change of ~ 3 mol%
592 An per kbar (Ustunisik et al., 2014), this would not explain the observed Cpx Mg#
593 zoning. It seems more likely that the multiple abrupt increases in An% content (up to
594 10%) from core to rim of oscillatory coarse banding are likely to be produced by the
595 same process as abrupt zoning in Cpx; magma mixing between more evolved and
596 primitive melts from the different magmatic environments.

597 Some oscillatory zoning in Pl phenocrysts record at least three episodes of
598 compositional variations (i.e., Fig.S10a), indicating that they have undergone at least
599 three regularly paced small injections of magmas that were slightly hotter and more
600 compositionally primitive than the Pl growth environment (Ginibre et al., 2002; van
601 Gerve et al., 2020). Compared with the coarse oscillatory banding, the fine oscillatory
602 zoning with low-amplitude anorthite content (0-3 An%) and short width (< 20 μm) (i.e.,
603 Figs.S11b, S11c) may be largely attributed to crystallization kinetics (Ginibre et al.,

604 2002; Loomis, 1982; Tsune and Toramaru, 2007) and crystallization in a stable magma
605 reservoir with stable oxidation conditions according to the stable Fe contents in fine
606 oscillatory zoning (Tapu et al., 2022). However, we cannot rule out the possibility that
607 such fine-scale zoning also records frequent, small-volume injections of new magma
608 into the reservoir, which could produce subtle chemical variations without forming
609 coarse oscillatory bands. Repeated smaller injections could perhaps account for some
610 of the 'spikeyness' in the profiles for Cr and Ti in Cpx (Fig.11), that is smeared away
611 by faster diffusion of Fe-Mg so not seen in Mg# transects.
612
613 5.3 In-situ Sr isotopes in Pl and their implications on the petrogenesis of Site 1578
614 basalts
615 Whole-rock Sr-Nd-Pb-Hf-La-Ce-O isotopic data of rocks from Tristan-Gough
616 hotspot track have revealed that the underlying plume structure is likely sourced from
617 a heterogeneous lower mantle region, containing contributions from EM1-type mantle
618 (Boyet et al., 2019; Gibson et al., 2005; Harris et al., 2000; Hoernle et al., 2015;
619 Homrighausen et al., 2019; Homrighausen et al., 2020; Salters and Sachi-Kocher, 2010;
620 Willbold and Stracke, 2010). As we discussed above, however, magma bodies in the
621 crust result from mixing of multiple batches of mantle-derived magmas (Batiza, 1984;
622 Cipriani et al., 2004), and the degree to which we can reconstruct the heterogeneity in
623 mantle source regions from basalts is uncertain (Lambart et al., 2019). Moreover,
624 conducting systematic geochemical analyses from the lower to upper igneous units at
625 one drill site can shed new light on mantle heterogeneity on the centimeter to kilometer

scale (Lambart et al., 2019; Lissenberg et al., 2024) and help us determine the temporal geochemical evolution of the mantle source (Höfig et al., 2014; Sano et al., 2011).

In this study, Site U1578 Pl are isotopically heterogeneous, with a clear contrast between upper and lower units (Fig.12; upper = ~0.7044±0.0001; lower = ~0.7040± 0.0001). These $^{87}Sr/^{86}Sr$ values are significantly higher than those from basalts from South Mid-Atlantic Ridge (SMAR; $^{87}Sr/^{86}Sr$ = 0.7030-0.7035; Castillo and Batiza, 1989; Fontignie and Schilling, 1996; Graham et al., 1996; Ito et al., 1987; Regelous et al., 2009; Zhang et al., 2021). Within a single crystal, variations are mostly unresolvable within analytical uncertainty (Fig.S11). To assess whether the $^{87}Sr/^{86}Sr$ variations in Pl between different depth intervals are statistically significant, we performed two-sample t-tests for all possible pairs of Pl grains from nine core sections (see Table S5). The results are visualized in a heatmap (Fig.S12), where pairwise comparisons with p-values < 0.05 indicate statistically significant differences. The five deepest samples (37-60 R) are all significantly different from the four upper samples (22R-29R). When considering all measurements within the upper vs. lower units, these are also statistically different with p-values < 0.05.

We wish to investigate the origin of these differences between lower and upper units. Sr isotopes can be modified when Pl are metasomatically altered by seawater. However, the combination of low loss on ignition (LOI) contents (Table S1A) and petrographic observations indicating fresh mineral phenocrysts (Figs.3, S13) suggests minimal secondary overprint, indicating that $^{87}Sr/^{86}Sr$ ratio in the Pl is likely to retain primary magmatic signatures. Moreover, the lack of differences in LOI contents

between the lower and upper units further indicates that the significant Sr isotopic variations are not attributable to alteration. Considering the slow diffusion rate of Sr in Pl and the relatively short residence time in the magma reservoirs of intraplate volcanoes (Costa et al., 2020), we infer that their $^{87}Sr/^{86}Sr$ ratios are unlikely to be significantly modified through reequilibration with the host melt. Thus, it seems likely that the shift towards more radiogenic Sr isotopes in the upper units do reflect the infiltration of higher $^{87}Sr/^{86}Sr$ isotopic components in the crust or plume itself (Edwards et al., 2019; Waight and Tørnqvist, 2018).

It is still unclear whether the Center track represents a distinct geochemical end member or simply represents mixing between the Tristan- and Gough-type (Sager and Hoernle, 2022). To further explore the contribution of Tristan and Gough tracks to the Center track, we compare our data with the published Sr isotope ratios of volcanic rocks along the Tristan and Gough tracks (Hoernle et al., 2015; Rohde et al., 2013a; Salters and Sachi-Kocher, 2010). Plagioclases from lower igneous units of Site U1578 have significantly lower Sr isotope ratios than Gough track samples, but plot within the range of the Tristan track samples from DSDP Sites 527 and 528 (Fig.13a), indicating they may share similar sources with Tristan track samples. We propose that the shift to more radiogenic Sr from lower to upper igneous units is likely attributed to incorporation of more radiogenic Gough-type components into the plume source, rather than a process occurring in the crust beneath Walvis Ridge. However, more work is required to test this idea further (i.e., Nd-Hf-Pb isotope). It should be noted that the presence of sedimentary interbeds (Figs.2, 12), and magnetic reversals recorded within Site U1578

(Sager and Hoernle, 2022) imply episodic volcanism over an extended period (>2 Myrs) (Knight et al., 2004; Potter et al., 2019). Although the whole-rock compositions between upper and lower igneous units show no obvious differences (Fig.4), Ol from upper igneous units are characterized by higher Fo, NiO contents and crystallization temperature (Figs.5, 10), indicating that waning activity on the center track is characterized by eruption of magma carrying primitive crystal cargoes.

In conclusion, our in-situ Sr isotope data in Pl favor a hotspot/mantle plume origin for the Center track, given their similarity to the Tristan track and deviation from MORB. Additionally, Pl from Center track is broadly similar to those of Tristan-type end-member, but the shift to more radiogenic Sr isotopic signatures from the lower to the upper igneous units suggests an increasing contribution of radiogenic melts into the volcanic plumbing system, potentially derived from an increased supply of material from the Gough-type end-member and/or changes in the supply of melts from distinct mantle sources due to variations in melting conditions (i.e., lower mantle Tp).

5.4 The complex magmatic plumbing system beneath the Center track

Based on the lines of evidence discussed above, we proposed that three different magmatic environments were present beneath the Center track (Fig.14). The diverse zoning patterns of Cpx reveal a complex magmatic plumbing system beneath the Center track, involving processes such as fractional crystallization, magma mixing, recharge, and ascent. Multi-stage magma recharge is consistent with the observed chemical zoning patterns and Sr isotope compositions in Pl phenocrysts. To better constrain the

692 relative mixing of different mantle-derived melts contributing to different magmatic
693 systems (upper vs lower), we apply a quantitative binary mixing model using Sr
694 isotopic composition versus whole-rock Ba/Sr ratios for samples with LOI < 3 wt.%
695 (Table S6). We selected the most isotopically enriched and depleted whole-rock
696 compositions from 58-72 Ma Tristan-Gough tracks as endmembers (Homrighausen et
697 al., 2019; Rohde et al., 2013a). Sr and Ba exhibit similar geochemical behavior in
698 basalts and have comparable mineral-melt partition coefficients (Philpotts and
699 Schnetzler, 1970), therefore, their ratio is only minimally affected by fractional
700 crystallization. The whole-rock Sr isotope-Ba/Sr mixing diagram (Fig.13b) shows that
701 Tristan track samples are characterized by isotopically depleted values, whereas Gough
702 track samples are marked by enriched isotope ratios. For the Center track samples,
703 results indicate that the upper units (0.7042-0.7046) require 20-30% contribution from
704 the enriched Gough melts, whereas the lower units (0.7038-0.7042) require only 10%.
705 This implies that the upper units incorporated 10-20% more of melts from the enriched
706 Gough component relative to the lower units and variations in the contribution of
707 isotopically enriched melts played a key role in shaping the temporal and compositional
708 evolution of the Center track lavas.

709 Furthermore, the potential influence of the South Mid-Atlantic Ridge on the
710 Center track should not be overlooked. Notably, the $^{87}Sr/^{86}Sr$ values and An contents of
711 the Pl crystal in Sample 82 deviate markedly from the binary mixing trends (Fig. S2C)
712 towards lower $^{87}Sr/^{86}Sr$ ratios. In addition, in binary compositional plots (Figs.5, 6), 19
713 Ol and 6 Sp analyses fall within the typical MORB fields. We suggest that these crystals

714 are most likely inherited as scavenged xenocrysts from the Atlantic lower crust, rather
715 than crystallized from the Center track parental magma. Petrographic observations
716 reveal that the Pl crystal was larger (~0.8 cm) than other Pl phenocrysts (~0.2 cm) and
717 display corroded margins (Fig.S13C), indicating reaction with the host basaltic liquid
718 (Sial, 1977). Moreover, the occurrence of crystal clots within the same thin section (<2
719 cm apart; Fig.S13C) further supports the interpretation that numerous captured crystals
720 were entrained during magma ascent (Lissenberg et al., 2019; Sano et al., 2011). Taken
721 together, we infer that the occurrence of these anomalous mineral crystals in Sample 82
722 does not indicate direct involvement of South Mid-Atlantic Ridge-derived melts, but
723 rather represents the participation of lower oceanic crustal material into the magmatic
724 system beneath the Center track of Walvis Ridge.
725
726 **6. Conclusions**
727 We present the major, trace element, and Sr isotope data for Ol, Cpx, and Pl at Site
728 U1578 to elucidate the origin of magmatism in the Center track of Walvis Ridge and its
729 complex magmatic plumbing system. Our results lead to the following conclusions:
730 (1) Based on the Ol-Sp thermometry and pyMelt modeling, the calculated mantle
731 potential temperature of the Center track is at least 1400 °C, about 50 °C higher than
732 that of MORB, most likely reflecting the influence of a mantle plume.
733 (2) Based on the Cpx Mg# values and trace element compositions, three distinct
734 Cpx groups are identified. Diverse zoning in Cpx and Pl indicates that multi-stage
735 magma recharges and magma mixing are common magmatic processes within the

plumbing system beneath the Center track of Walvis Ridge.

(3) Site U1578 Pl are isotopically heterogeneous (0.7038 ± 0.0001 to 0.7046 ± 0.0001) and broadly similar to those of Tristan-type end-member. The shift to more radiogenic Sr isotopic signatures from the lower to the upper igneous units suggests the increasing incorporation of radiogenic materials into the mantle source, potentially derived from the Gough-type end-member. This study helps us determine the temporal geochemical evolution of mantle source heterogeneity beneath the Center track of Walvis Ridge.

Declaration of Competing Interest

We have no known competing financial interests or personal relationships that could have appeared to influence the work reported in this paper.

Acknowledgments

The authors are grateful to all scientists on board Expedition 391 of the International Ocean Discovery Program, as well as the crew of the D/V *JOIDES Resolution* and the IODP technical staff for their role in obtaining samples. We thank Simon Matthews, Wei-Ran Li and Yishen Zhang for their valuable guidance on the pyMELT modeling and Ol-Sp thermometer. We thank Mihai Ducea and Shan Li for the editorial handling, Gang Zeng, and Tong Hou for their constructive comments that significantly improved this work. The authors are also grateful to the support of the Hainan Observation and Research Station of Ecological Environment and Fishery

Resource in Yazhou Bay. This study was supported by the National Key Research and Development Program of China (2023YFF0803404), the National Natural Science Foundation of China (Nos. 42072069 and 42176055), the Zhejiang University Seek Truth Eagle Scholarship (No. 12234074). EDS analyses were supported by an NSF IF grant 2218698 to MG and PW.

References (main text):

Anderson, D.L. and Natland, J.H., 2014. Mantle updrafts and mechanisms of oceanic volcanism. Proceedings of the National Academy of Sciences, 111(41): E4298-E4304.

Barker, A.K., Troll, V.R., Carracedo, J.C. and Nicholls, P.A., 2015. The magma plumbing system for the 1971 Teneguía eruption on La Palma, Canary Islands. Contributions to Mineralogy and Petrology, 170(5-6).

Barnes, S.J. and Roeder, P.L., 2001. The Range of Spinel Compositions in Terrestrial Mafic and Ultramafic Rocks. Journal of Petrology, 42(12): 2279-2302.

Batiza, R., 1984. Inverse relationship between Sr isotope diversity and rate of oceanic volcanism has implications for mantle heterogeneity. Nature, 309(5967): 440-441.

Baxter, R.J.M., Maclennan, J., Neave, D.A. and Thordarson, T., 2023. Depth of Magma Storage Under Iceland Controlled by Magma Fluxes. Geochemistry, Geophysics, Geosystems, 24(7).

Bennett, E.N., Jenner, F.E., Millet, M., Cashman, K.V. and Lissenberg, C.J., 2019. Deep roots for mid-ocean-ridge volcanoes revealed by plagioclase-hosted melt inclusions. Nature, 572(7768): 235-239.

Bonechi, B. et al., 2024. Magma residence time, ascent rate and eruptive style of the November ash-laden activity during the 2021 Tajogaite eruption (La Palma, Spain). Volcanica, 7(1): 51 - 65.

Boyet, M. et al., 2019. New Constraints on the Origin of the EM-1 Component Revealed by the Measurement of the La-Ce Isotope Systematics in Gough Island Lavas. Geochemistry, Geophysics, Geosystems, 20(5): 2484-2498.

Campbell, I.H. and Griffiths, R.W., 1990. Implications of mantle plume structure for the evolution of flood basalts. Earth and Planetary Science Letters, 99(1): 79-93.

Campbell, I.H. and Griffiths, R.W., 1992. The Changing Nature of Mantle Hotspots through Time: Implications for the Chemical Evolution of the Mantle. The Journal of Geology, 100(5): 497-523.

Cao, G., Xue, H. and Tong, Y., 2022. Complex magmatic processes recorded by clinopyroxene phenocrysts in a magmatic plumbing system: A case study of mafic volcanic rocks from the Laiyang Basin, southeastern North China Craton. Lithos, 416-417: 106673.

Carter, E.J. et al., 2024. Volcanic tempo driven by rapid fluctuations in mantle temperature during large igneous province emplacement. Earth and Planetary Science Letters, 644: 118903.

Cashman, K.V., Sparks, R.S.J. and Blundy, J.D., 2017. Vertically extensive and unstable magmatic systems: A unified view of igneous processes. Science, 355(6331).

Chen, S., Gao, R., Zheng, J. and Liu, J., 2023. Tectono-magmatic evolution of the Greenland–Iceland–Norway ridge complex and the Jan Mayen hotspot in the Arctic Atlantic Ocean: Constraints from in situ trace elements and Sr isotopes of minerals. GSA Bulletin.

Chen, S., Zhang, W., Dingwell, D.B., Gao, R. and Liu, J., 2024. Tectonic dismemberment and plume-ridge interaction in the Sub-Antarctic South Atlantic Ocean Basin: Confirmation from in situ geochemical and Sr isotopic compositions of minerals. GSA Bulletin.

Cipriani, A., Brueckner, H.K., Bonatti, E. and Brunelli, D., 2004. Oceanic crust generated by elusive parents: Sr and Nd isotopes in basalt-peridotite pairs from the Mid-Atlantic Ridge. Geology, 32(8): 657-660.

Class, C. and le Roex, A.P., 2008. Ce anomalies in Gough Island lavas — Trace element characteristics of a recycled sediment component. Earth and Planetary Science Letters, 265(3-4): 475-486.

Class, C., Koppers, A., Sager, W., Schnur, S. and Anonymous, 2015. Walvis Ridge-Tristan-Gough, South Atlantic; triple-zonation of a plume over 60 Ma and the role of LLSVP. V.M. Goldschmidt Conference - Program and Abstracts, 25: 568.

Cliff, R.A., Baker, P.E. and Mateer, N.J., 1991. Geochemistry of inaccessible island volcanics. Chemical Geology, 92(4): 251-260.

Contreras, E. et al., 2022. Bathymetry of Valdivia Bank, Walvis Ridge, South Atlantic Ocean: Implications for Structure and Geologic History of a Hot Spot Plateau. Geochemistry, Geophysics, Geosystems, 23(11).

Coogan, L.A., Saunders, A.D. and Wilson, R.N., 2014. Aluminum-in-olivine thermometry of primitive basalts: Evidence of an anomalously hot mantle source for large igneous provinces. Chemical Geology, 368: 1-10.

Cooper, K.M., 2017. What Does a Magma Reservoir Look Like? The “Crystal's-Eye” View. Elements, 13(1): 23-28.

Costa, F., Shea, T. and Ubide, T., 2020. Diffusion chronometry and the timescales of magmatic processes. Nature Reviews Earth & Environment, 1(4): 201-214.

DeVitre, C.L. et al., 2024. Depths in a day — A new era of rapid-response Raman-based barometry using fluid inclusions. Journal of Petrology: egae119.

Di Stefano, F. et al., 2020. Mush cannibalism and disruption recorded by clinopyroxene phenocrysts at Stromboli volcano: New insights from recent 2003–2017 activity. Lithos, 360-361: 105440.

Dimanov, A. and Wiedenbeck, M., 2006. (Fe,Mn)-Mg interdiffusion in natural diopside: effect of pO2. European Journal of Mineralogy, 18(6): 705-718.

Downes, M.J., 1974. Sector and oscillatory zoning in calcic augites from M. Etna, Sicily. Contributions to Mineralogy and Petrology, 47(3): 187-196.

Drignon, M.J., Nielsen, R.L., Tepley, F.J. and Bodnar, R.J., 2019. Reequilibration Processes Occurring in Plagioclase-Hosted Melt Inclusions From Plagioclase Ultraphyric Basalts. Geochemistry, Geophysics, Geosystems, 20(1): 109-119.

Duncan, R.A. and Richards, M.A., 1991. Hotspots, mantle plumes, flood basalts, and true polar wander. Reviews of Geophysics, 29(1): 31-50.

Edwards, M.A. et al., 2019. Extreme enriched and heterogeneous 87Sr/86Sr ratios recorded in magmatic plagioclase from the Samoan hotspot. Earth and Planetary Science Letters, 511: 190-201.

EWART, A. et al., 2004. Petrology and Geochemistry of Early Cretaceous Bimodal Continental Flood Volcanism of the NW Etendeka, Namibia. Part 1: Introduction, Mafic Lavas and Re-evaluation of Mantle Source Components. Journal of Petrology, 45(1): 59-105.

Ganne, J., Bachmann, O. and Feng, X., 2018. Deep into magma plumbing systems: Interrogating the crystal cargo of volcanic deposits. Geology, 46(5): 415-418.

Gazel, E. et al., 2025. Crustal to mantle melt storage during the evolution of Hawaiian volcanoes. Science

Advances, 11(20): eadu9332.
Geissler, W.H., Jokat, W., Jegen, M. and Baba, K., 2017. Thickness of the oceanic crust, the lithosphere, and the mantle transition zone in the vicinity of the Tristan da Cunha hot spot estimated from ocean-bottom and ocean-island seismometer receiver functions. Tectonophysics, 716: 33-51.
Giacomoni, P.P. et al., 2021. Thermo-barometric constraints on the Mt. Etna 2015 eruptive event. Contributions to Mineralogy and Petrology, 176(11).
Giacomoni, P.P., Coltorti, M., Bryce, J.G., Fahnestock, M.F. and Guitreau, M., 2016. Mt. Etna plumbing system revealed by combined textural, compositional, and thermobarometric studies in clinopyroxenes. Contributions to Mineralogy and Petrology, 171(4).
Gibson, S.A., Thompson, R.N., Day, J.A., Humphris, S.E. and Dickin, A.P., 2005. Melt-generation processes associated with the Tristan mantle plume: Constraints on the origin of EM-1. Earth and Planetary Science Letters, 237(3-4): 744-767.
Ginibre, C., Kronz, A. and Wörner, G., 2002. High-resolution quantitative imaging of plagioclase composition using accumulated backscattered electron images: new constraints on oscillatory zoning. Contributions to Mineralogy and Petrology, 142(4): 436-448.
Ginibre, C., Wörner, G. and Kronz, A., 2007. Crystal Zoning as an Archive for Magma Evolution. Elements, 3(4): 261-266.
Gleeson, M. et al., 2025. Persistent High-Pressure Magma Storage beneath a Near-Ridge Ocean Island Volcano (Isla Floreana, Galápagos). Journal of Petrology, 66(5): egaf031.
Gleeson, M.L.M., Gibson, S.A. and Stock, M.J., 2020. Upper Mantle Mush Zones beneath Low Melt Flux Ocean Island Volcanoes: Insights from Isla Floreana, Galápagos. Journal of Petrology, 61(11-12).
Harris, C., Smith, H.S. and le Roex, A.P., 2000. Oxygen isotope composition of phenocrysts from Tristan da Cunha and Gough Island lavas: variation with fractional crystallization and evidence for assimilation. Contributions to Mineralogy and Petrology, 138(2): 164-175.
Herzberg, C., 2011. Basalts as temperature probes of Earth's mantle. Geology, 39(12): 1179-1180.
Herzberg, C. and Asimow, P.D., 2008. Petrology of some oceanic island basalts: PRIMELT2.XLS software for primary magma calculation. Geochemistry, Geophysics, Geosystems, 9(9).
Hirano, N. et al., 2019. Petit-spot volcanoes on the oldest portion of the Pacific plate. Deep Sea Research Part I: Oceanographic Research Papers, 154: 103142.
Hoernle, K. et al., 2015. How and when plume zonation appeared during the 132 Myr evolution of the Tristan Hotspot. Nature Communications, 6(1).
Höfig, T.W. et al., 2014. From the lavas to the gabbros: 1.25km of geochemical characterization of upper oceanic crust at ODP/IODP Site 1256, eastern equatorial Pacific. Lithos, 210-211: 289-312.
Hofmann, A.W. and White, W.M., 1982. Mantle plumes from ancient oceanic crust. Earth and Planetary Science Letters, 57(2): 421-436.
Homrighausen, S. et al., 2018. Unexpected HIMU-type late-stage volcanism on the Walvis Ridge. Earth and Planetary Science Letters, 492: 251-263.
Homrighausen, S. et al., 2019. New age and geochemical data from the Walvis Ridge: The temporal and spatial diversity of South Atlantic intraplate volcanism and its possible origin. Geochimica et Cosmochimica Acta, 245: 16-34.
Homrighausen, S. et al., 2020. Paired EMI-HIMU hotspots in the South Atlantic-Starting plume heads trigger compositionally distinct secondary plumes? Science Advances, 6(28): eaba0282.
Homrighausen, S. et al., 2023. Evidence for compositionally distinct upper mantle plumelets since the early history of the Tristan-Gough hotspot. Nature Communications, 14(1).

Huang, L. and Li, C., 2024. What controls the magma production rate along the Walvis Ridge, South Atlantic? Tectonophysics: 230381.

Jankovics, M.É. et al., 2016. Clinopyroxene with diverse origins in alkaline basalts from the western Pannonian Basin: Implications from trace element characteristics. Lithos, 262: 120-134.

Jennings, E.S., Gibson, S.A. and Maclennan, J., 2019. Hot primary melts and mantle source for the Paraná-Etendeka flood basalt province: New constraints from Al-in-olivine thermometry. Chemical Geology, 529: 119287.

Jerram, D.A. and Martin, V.M., 2008. Understanding crystal populations and their significance through the magma plumbing system. Geological Society Special Publication, 304: 133-148.

Johnson, D., Hooper, P. and Conrey, R., 1999. XRF method XRF analysis of rocks and minerals for major and trace elements on a single low dilution Li-tetraborate fused bead. Advances in X-ray Analysis, 41: 843-867.

Kamenetsky, V.S., Crawford, A.J. and Meffre, S., 2001. Factors Controlling Chemistry of Magmatic Spinel: an Empirical Study of Associated Olivine, Cr-spinel and Melt Inclusions from Primitive Rocks. Journal of Petrology, 42(4): 655-671.

Katz, R.F., Spiegelman, M. and Langmuir, C.H., 2003. A new parameterization of hydrous mantle melting. Geochemistry, Geophysics, Geosystems, 4(9).

Klügel, A., Day, S., Schmid, M. and Faria, B., 2020. Magma Plumbing During the 2014–2015 Eruption of Fogo (Cape Verde Islands). Frontiers in Earth Science, 8.

Knight, K.B. et al., 2004. The Central Atlantic Magmatic Province at the Triassic–Jurassic boundary: paleomagnetic and 40Ar/39Ar evidence from Morocco for brief, episodic volcanism. Earth and Planetary Science Letters, 228(1): 143-160.

Kogiso, T., Hirose, K. and Takahashi, E., 1998. Melting experiments on homogeneous mixtures of peridotite and basalt: application to the genesis of ocean island basalts. Earth and Planetary Science Letters, 162(1): 45-61.

Kouchi, A., Sugawara, Y., Kashima, K. and Sunagawa, I., 1983. Laboratory growth of sector zoned clinopyroxenes in the system CaMgSi2O6-CaTiAl2O6. Contributions to Mineralogy and Petrology, 83: 177-184.

Lambart, S. et al., 2019. Highly heterogeneous depleted mantle recorded in the lower oceanic crust. Nature Geoscience, 12(6): 482-486.

Lange, A.E., Nielsen, R.L., Tepley, F.J.I. and Kent, A.J.R., 2013. Diverse Sr isotope signatures preserved in mid-oceanic-ridge basalt plagioclase. Geology, 41(2): 279-282.

Le Roex, A.P., 1985. Geochemistry, Mineralogy and Magmatic Evolution of the Basaltic and Trachytic Lavas from Gough Island, South Atlantic. Journal of Petrology, 26(1): 149-186.

Le Roex, A.P., Cliff, R.A. and Adair, B.J.I., 1990. Tristan da Cunha, South Atlantic; geochemistry and petrogenesis of a basanite-phonolite lava series. Journal of petrology, 31(4): 779-812.

Leung, I.S., 1974. Sector-zoned titanaugites: morphology, crystal chemistry, and growth. American Mineralogist, 59(1-2): 127-138.

Li, W. et al., 2025. Taking the temperature of ocean islands: a petrological approach. Journal of Petrology: egaf033.

Li, X. et al., 2020. Integrated major and trace element study of clinopyroxene in basic, intermediate and acidic volcanic rocks from the middle Okinawa Trough: Insights into petrogenesis and the influence of subduction component. Lithos, 352-353: 105320.

Lissenberg, C.J. et al., 2024. A long section of serpentinized depleted mantle peridotite. Science,

385(6709): 623-629.
Lissenberg, C.J., MacLeod, C.J. and Bennett, E.N., 2019. Consequences of a crystal mush-dominated magma plumbing system: a mid-ocean ridge perspective. Philosophical Transactions of the Royal Society A: Mathematical, Physical and Engineering Sciences, 377(2139): 20180014.
Liu, S., Zheng, Y., Hou, Z. and Shen, Y., 2022. Multi-stage crustal magma reservoirs of ultrapotassic rocks recorded by zoned clinopyroxene. Journal of Asian Earth Sciences, 226: 105072.
Liu, Y. et al., 2008. In situ analysis of major and trace elements of anhydrous minerals by LA-ICP-MS without applying an internal standard. Chemical Geology, 257(1-2): 34-43.
Loomis, T.P., 1982. Numerical simulations of crystallization processes of plagioclase in complex melts: the origin of major and oscillatory zoning in plagioclase. Contributions to Mineralogy and Petrology, 81(3): 219-229.
Lynn, K.J. et al., 2024. Triggering the 2022 eruption of Mauna Loa. Nature Communications, 15(1).
Ma, B. et al., 2024. Trans-Lithospheric Ascent Processes of the Deep-Rooted Magma Plumbing System Underneath the Ultraslow-Spreading SW Indian Ridge. Journal of Geophysical Research: Solid Earth, 129(1): e2023JB027224.
Ma, R. et al., 2024. Magmatic processes in the plumbing system of the Cenozoic ultrapotassic volcanic rocks in the southeastern Tibetan Plateau. GSA Bulletin.
Masotta, M. et al., 2020. The role of undercooling during clinopyroxene growth in trachybasaltic magmas: Insights on magma decompression and cooling at Mt. Etna volcano. Geochimica et Cosmochimica Acta, 268: 258-276.
Matthews, S., Shorttle, O. and Maclennan, J., 2016. The temperature of the Icelandic mantle from olivine-spinel aluminum exchange thermometry. Geochemistry, Geophysics, Geosystems, 17(11): 4725-4752.
Matthews, S., Wong, K. and Gleeson, M., 2022. pyMelt: An extensible Python engine for mantle melting calculations. Volcanica, 5(2): 469 - 475.
Matthews, S., Wong, K., Shorttle, O., Edmonds, M. and Maclennan, J., 2021. Do Olivine Crystallization Temperatures Faithfully Record Mantle Temperature Variability? Geochemistry, Geophysics, Geosystems, 22(4).
McDonough, W.F. and Sun, S.S., 1995. The composition of the Earth. Chemical Geology, 120(3): 223-253.
Molendijk, S.M., Buchs, D.M., Mason, P.R.D. and Blundy, J.D., 2022. Clinopyroxene diversity and magma plumbing system processes in an accreted Pacific ocean island, Panama. Contributions to Mineralogy and Petrology, 177(2): 30.
Mollo, S., Del Gaudio, P., Ventura, G., Iezzi, G. and Scarlato, P., 2010. Dependence of clinopyroxene composition on cooling rate in basaltic magmas: Implications for thermobarometry. Lithos, 118(3-4): 302-312.
Mollo, S., Ubide, T., Di Stefano, F., Nazzari, M. and Scarlato, P., 2020. Polybaric/polythermal magma transport and trace element partitioning recorded in single crystals: A case study of a zoned clinopyroxene from Mt. Etna. Lithos, 356-357: 105382.
Morgan, W.J., 1971. Convection Plumes in the Lower Mantle. Nature, 230(5288): 42-43.
Morimoto, N. et al., 1988. Nomenclature of Pyroxenes. Mineralogical Magazine, 52(367): 535-550.
Müller, T., Dohmen, R., Becker, H.W., ter Heege, J.H. and Chakraborty, S., 2013. Fe–Mg interdiffusion rates in clinopyroxene: experimental data and implications for Fe–Mg exchange geothermometers. Contributions to Mineralogy and Petrology, 166(6): 1563-1576.

Mutch, E.J.F., Maclennan, J., Holland, T.J.B. and Buisman, I., 2019. Millennial storage of near-Moho magma. Science, 365(6450): 260-264.

Nardini, N. et al., 2024. Modelling ancient magma plumbing systems through clinopyroxene populations: a case study from Middle Triassic volcanics (Dolomites, Italy). Contributions to Mineralogy and Petrology, 179(3).

Neave, D.A., Beckmann, P., Behrens, H. and Holtz, F., 2021. Mixing between chemically variable primitive basalts creates and modifies crystal cargoes. Nature Communications, 12(1).

O'Connor, J.M. and Jokat, W., 2015a. Age distribution of Ocean Drill sites across the Central Walvis Ridge indicates plate boundary control of plume volcanism in the South Atlantic. Earth and Planetary Science Letters, 424: 179-190.

O'Connor, J.M. and Jokat, W., 2015b. Tracking the Tristan-Gough mantle plume using discrete chains of intraplate volcanic centers buried in the Walvis Ridge. Geology, 43(8): 715-718.

Palin, R.M. and Santosh, M., 2021. Plate tectonics: What, where, why, and when? Gondwana Research, 100: 3-24.

Palummo, F. et al., 2021. Decoding multiple zoning patterns in clinopyroxene phenocrysts at Vulcano Island: A record of dynamic crystallization through interconnected reservoirs. Lithos, 406-407: 106517.

Pedregosa, F. et al., 2011. Scikit-learn: Machine learning in Python. the Journal of machine Learning research, 12: 2825-2830.

Pelullo, C. et al., 2022. Insights into the temporal evolution of magma plumbing systems from compositional zoning in clinopyroxene crystals from the Agnano-Monte Spina Plinian eruption (Campi Flegrei, Italy). Geochimica et Cosmochimica Acta, 328: 185-206.

Peslier, A.H., Bizimis, M. and Matney, M., 2015. Water disequilibrium in olivines from Hawaiian peridotites: Recent metasomatism, H diffusion and magma ascent rates. Geochimica et Cosmochimica Acta, 154: 98-117.

Petrone, C.M. et al., 2022. Magma recharge and mush rejuvenation drive paroxysmal activity at Stromboli volcano. Nature Communications, 13(1).

Petrone, C.M., Braschi, E., Francalanci, L., Casalini, M. and Tommasini, S., 2018. Rapid mixing and short storage timescale in the magma dynamics of a steady-state volcano. Earth and Planetary Science Letters, 492: 206-221.

Philpotts, J.A. and Schnetzler, C.C., 1970. Phenocryst-matrix partition coefficients for K, Rb, Sr and Ba, with applications to anorthosite and basalt genesis. Geochimica et Cosmochimica Acta, 34(3): 307-322.

Potter, K.E., Champion, D.E., Duncan, R.A. and Shervais, J.W., 2019. Volcanic stratigraphy and age model of the Kimama deep borehole (Project Hotspot): Evidence for 5.8 million years of continuous basalt volcanism, central Snake River Plain, Idaho. Geosphere, 15(3): 736-758.

Putirka, K.D., 2005. Mantle potential temperatures at Hawaii, Iceland, and the mid-ocean ridge system, as inferred from olivine phenocrysts: Evidence for thermally driven mantle plumes. Geochemistry, Geophysics, Geosystems, 6(5).

Putirka, K.D., Mikaelian, H., Ryerson, F. and Shaw, H., 2003. New clinopyroxene-liquid thermobarometers for mafic, evolved, and volatile-bearing compositions, with applications to lavas from Tibet and the Snake River Plain, Idaho. American Mineralogist, 88(10): 1542.

Ren, Z.Y., Takahashi, E., Orihashi, Y. and Johnson, K.T.M., 2004. Petrogenesis of tholeiitic lavas from the submarine Hana Ridge, Haleakala volcano, Hawaii. Journal of Petrology, 45(10): 2067-2099.

Renne, P.R., Glen, J.M., Milner, S.C. and Duncan, A.R., 1996. Age of Etendeka flood volcanism and associated intrusions in southwestern Africa. Geology, 24(7): 659-662.

Richards, M.A., Duncan, R.A. and Courtillot, V.E., 1989. Flood Basalts and Hot-Spot Tracks: Plume Heads and Tails. Science, 246(4926): 103-107.

Rohde, J.K. et al., 2013a. 70 Ma chemical zonation of the Tristan-Gough hotspot track. Geology, 41(3): 335-338.

Rohde, J.K., van den Bogaard, P., Hoernle, K., Hauff, F. and Werner, R., 2013b. Evidence for an age progression along the Tristan-Gough volcanic track from new 40Ar/39Ar ages on phenocryst phases. Tectonophysics, 604: 60-71.

Sager, W. and Hoernle, K., 2022. Expedition 391 Preliminary Report: Walvis Ridge Hotspot: Drilling Walvis Ridge, Southeast Atlantic Ocean, to Test Models of Ridge-Hotspot Interaction, Isotopic Zonation, and the Hotspot Reference Frame. International Ocean Discovery Program.

Sager, W.W., Thoram, S., Engfer, D.W., Koppers, A.A.P. and Class, C., 2021. Late Cretaceous Ridge Reorganization, Microplate Formation, and the Evolution of the Rio Grande Rise – Walvis Ridge Hot Spot Twins, South Atlantic Ocean. Geochemistry, Geophysics, Geosystems, 22(3).

Salters, V.J.M. and Sachi-Kocher, A., 2010. An ancient metasomatic source for the Walvis Ridge basalts. Chemical Geology, 273(3-4): 151-167.

Sano, T., Sakuyama, T., Ingle, S., Rodriguez, S. and Yamasaki, T., 2011. Petrological relationships among lavas, dikes, and gabbros from Integrated Ocean Drilling Program Hole 1256D: Insight into the magma plumbing system beneath the East Pacific Rise. Geochemistry, Geophysics, Geosystems, 12(6): n/a-n/a.

Schlömer, A., Geissler, W.H., Jokat, W. and Jegen, M., 2017. Hunting for the Tristan mantle plume – An upper mantle tomography around the volcanic island of Tristan da Cunha. Earth and Planetary Science Letters, 462: 122-131.

Scholpp, J.L. et al., 2022. Petrologic evolution of boninite lavas from the IBM Fore-arc, IODP Expedition 352: Evidence for open-system processes during early subduction zone magmatism. American Mineralogist, 107(4): 572-586.

Scholpp, J.L. et al., 2025. He Isotope Evidence of a Primitive Mantle Source Beneath the Tristan-Gough-Walvis Hotspot Track, Goldschmidt 2025 Conference. GOLDSCHMIDT.

Sial, A.N., 1977. Petrology and mineral chemistry of peridotite nodules included in Tertiary basaltic rocks of northeast Brazil. GSA Bulletin, 88(8): 1173-1176.

Spice, H.E., Fitton, J.G. and Kirstein, L.A., 2016. Temperature fluctuation of the Iceland mantle plume through time. Geochemistry, Geophysics, Geosystems, 17(2): 243-254.

Streck, M.J., 2008. Mineral Textures and Zoning as Evidence for Open System Processes. Reviews in Mineralogy and Geochemistry, 69(1): 595-622.

Sun, C. and Liang, Y., 2012. Distribution of REE between clinopyroxene and basaltic melt along a mantle adiabat: effects of major element composition, water, and temperature. Contributions to Mineralogy and Petrology, 163(5): 807-823.

Sun, S.S. and McDonough, W.F., 1989. Chemical and isotopic systematics of oceanic basalts: implications for mantle composition and processes. Geological Society, London, Special Publications, 42(1): 313-345.

Tapu, A.T., Ubide, T. and Vasconcelos, P.M., 2022. Plumbing System Architecture of Late-Stage Hotspot Volcanoes in Eastern Australia. Journal of Petrology, 63(3).

Thompson, R.N. and Gibson, S.A., 2000. Transient high temperatures in mantle plume heads inferred from magnesian olivines in Phanerezoic picrites. Nature, 407(6803): 502-506.

Thoram, S. et al., 2023. Nature and Origin of Magnetic Lineations Within Valdivia Bank: Ocean Plateau

Formation by Complex Seafloor Spreading. Geophysical Research Letters, 50(13).
Thoram, S., Sager, W.W. and Jokat, W., 2019. Implications of Updated Magnetic Anomalies for the Late Cretaceous Tectonic Evolution of Walvis Ridge. Geophysical Research Letters, 46(16): 9474-9482.
Tsune, A. and Toramaru, A., 2007. A simple model of oscillatory zoning in magmatic plagioclase: Development of an isothermal undercooling model. American Mineralogist, 92(7): 1071-1079.
Turcotte, D.L. et al., 1997. Intra-plate volcanism. Philosophical Transactions of the Royal Society of London. Series A, Mathematical and Physical Sciences, 288(1355): 561-579.
Ubide, T., Mollo, S., Zhao, J., Nazzari, M. and Scarlato, P., 2019. Sector-zoned clinopyroxene as a recorder of magma history, eruption triggers, and ascent rates. Geochimica et Cosmochimica Acta, 251: 265-283.
Ubide, T., Neave, D.A., Petrelli, M. and Longpré, M., 2021. Crystal Archives of Magmatic Processes. Frontiers in Earth Science, 9.
Ustunisik, G., Kilinc, A. and Nielsen, R.L., 2014. New insights into the processes controlling compositional zoning in plagioclase. Lithos, 200-201: 80-93.
van Gerve, T.D. et al., 2024. The origin and differentiation of CO2-rich primary melts in Ocean Island volcanoes: Integrating 3D X-ray tomography with chemical microanalysis of olivine-hosted melt inclusions from Pico (Azores). Journal of Petrology: egae006.
van Gerve, T.D., Neave, D.A., Almeev, R.R., Holtz, F. and Namur, O., 2020. Zoned Crystal Records of Transcrustal Magma Transport, Storage and Differentiation: Insights from the Shatsky Rise Oceanic Plateau. Journal of Petrology, 61(8).
Waight, T.E. and Tørnqvist, J.B., 2018. Sr isotope zoning in plagioclase from andesites at Cabo De Gata, Spain: Evidence for shallow and deep contamination. Lithos, 308-309: 159-167.
Wan, Z., Coogan, L.A. and Canil, D., 2008. Experimental calibration of aluminum partitioning between olivine and spinel as a geothermometer. American Mineralogist, 93(7): 1142-1147.
Wei, X., Zhang, Y., Shi, X., Castillo, P.R. and Xu, Y., 2022. Concurrent magma mixing and crystallization processes revealed by clinopyroxene macrocrysts from Lamont guyot lavas in NW Pacific. Lithos, 428-429: 106833.
Weit, A. et al., 2017. The magmatic system beneath the Tristan da Cunha Island: Insights from thermobarometry, melting models and geophysics. Tectonophysics, 716: 64-76.
Wieser, P.E. et al., 2021. Reconstructing Magma Storage Depths for the 2018 Kīlauean Eruption From Melt Inclusion CO2 Contents: The Importance of Vapor Bubbles. Geochemistry, Geophysics, Geosystems, 22(2).
Wieser, P.E., Gleeson, M.L.M., Matthews, S., DeVitre, C. and Gazel, E., 2024. Determining the pressure-temperature-composition (P-T-X) conditions of magma storage. Treatise on Geochemistry (Third Edition).
Willbold, M. and Stracke, A., 2006. Trace element composition of mantle end-members: Implications for recycling of oceanic and upper and lower continental crust. Geochemistry, Geophysics, Geosystems, 7(4).
Willbold, M. and Stracke, A., 2010. Formation of enriched mantle components by recycling of upper and lower continental crust. Chemical Geology, 276(3-4): 188-197.
Williams, M. et al., 2020. pyrolite: Python for geochemistry. The Journal of Open Source Software, 5: 2314.
Wilson, J.T., 1963. A POSSIBLE ORIGIN OF THE HAWAIIAN ISLANDS. Canadian Journal of Physics, 41(6): 863-870.

Wilson, J.T., 1973. Mantle plumes and plate motions. Tectonophysics, 19(2): 149-164.
Wu, T. et al., 2023. Highly unradiogenic Pb isotopes revealed by plagioclase-hosted melt inclusions in E-MORB from the South China Sea. Journal of Geophysical Research: Solid Earth, n/a(n/a): e2022JB025348.
Xu, L. et al., 2022. A natural plagioclase reference material for microbeam Sr isotopic analysis. Journal of Analytical Atomic Spectrometry, 37(8): 1706-1714.
Xu, R. and Liu, Y., 2016. Al-in-olivine thermometry evidence for the mantle plume origin of the Emeishan large igneous province. Lithos, 266-267: 362-366.
Yang, F., Huang, X., Xu, Y. and He, P., 2019. Magmatic Processes Associated with Oceanic Crustal Accretion at Slow-spreading Ridges: Evidence from Plagioclase in Mid-ocean Ridge Basalts from the South China Sea. Journal of Petrology, 60(6): 1135-1162.
Yang, Y., Wu, F., Xie, L., Yang, J. and Zhang, Y., 2009. In-situ Sr isotopic measurement of natural geological samples by LA-MC-ICP-MS. Acta Petrologica Sinica, 25(12): 3431-3441.
Zhang, G. et al., 2024. Multiple magmatic processes revealed by distinct clinopyroxene populations in the magma plumbing system: A case study from a Miocene volcano in West Qinling, Central China. American Mineralogist, 109(3): 540-555.
Zhang, L. et al., 2023. The effect of elemental diffusion on the application of olivine-composition-based magmatic thermometry, oxybarometry, and hygrometry: A case study of olivine phenocrysts from the Jiagedaqi basalts, northeast China. American Mineralogist, 108(8): 1449-1460.
Zhang, Y. et al., 2023. An extended calibration of the olivine–spinel aluminum exchange thermometer: Application to the melting conditions and mantle lithologies of large igneous provinces. Journal of Petrology: egad077.
Zhu, H. et al., 2024. Large Igneous Province magma plumbing system processes: insights from mineral chemistry and diffusion chronometry from the Shatsky Rise Oceanic Plateau, Northwest Pacific. Bulletin of Volcanology, 87(1): 5.

Figure and Table Captions

https://doi.org/10.1130/B38890.1

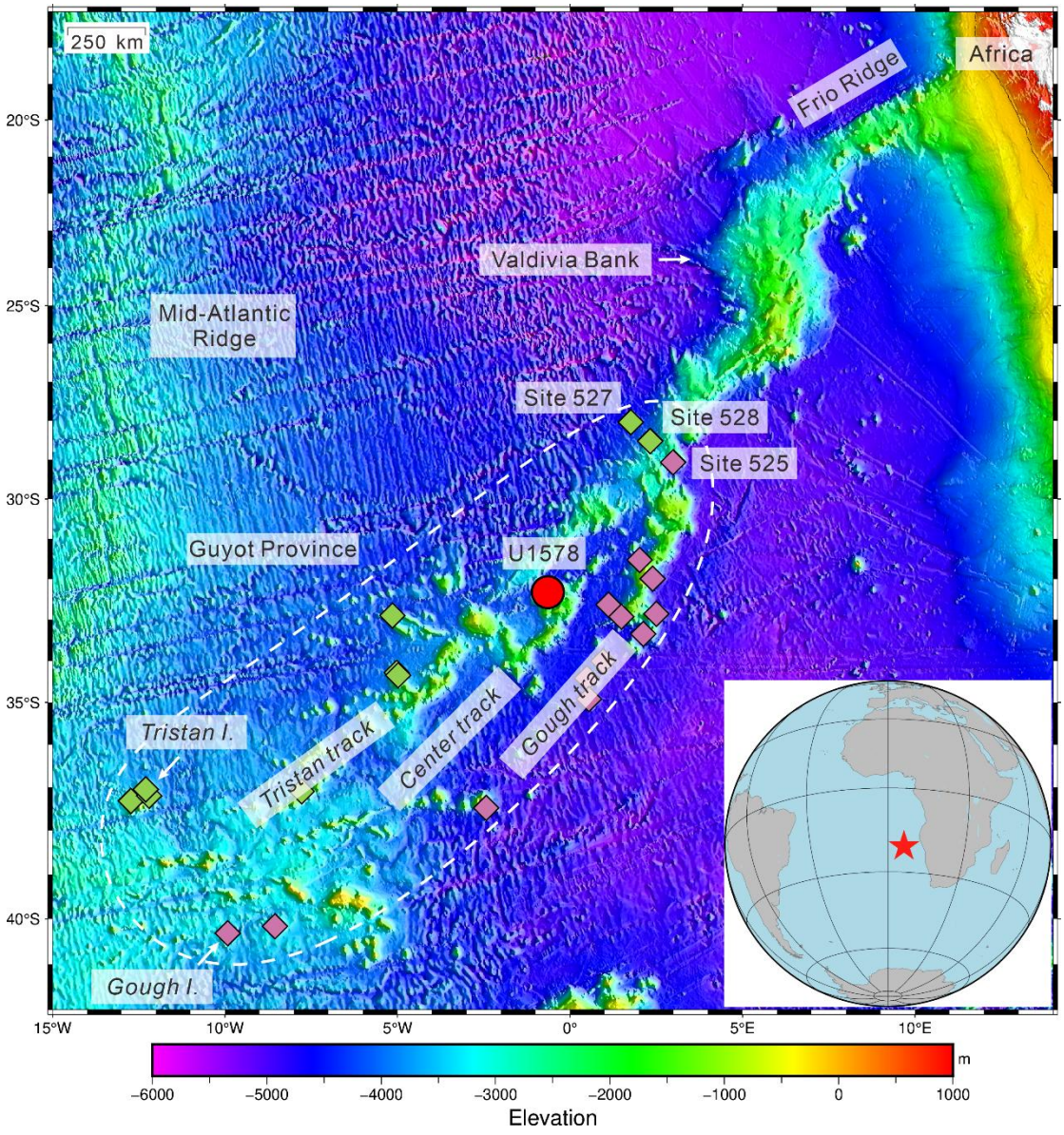

Fig. 1 Walvis Ridge bathymetry and feature names with the location of IODP Site U1578 (Sager and Hoernle, 2022). Inset shows the location of Walvis Ridge relative to the South Atlantic modified after Thoram, S., et al. (2013). The green and purple diamonds represent the locations of previous studies from Tristan track and Gough track (Hoernle et al., 2015; Homrighausen et al., 2019; Rohde et al., 2013a; Rohde et al., 2013b; Salters and Sachi-Kocher, 2010).

https://doi.org/10.1130/B38890.1

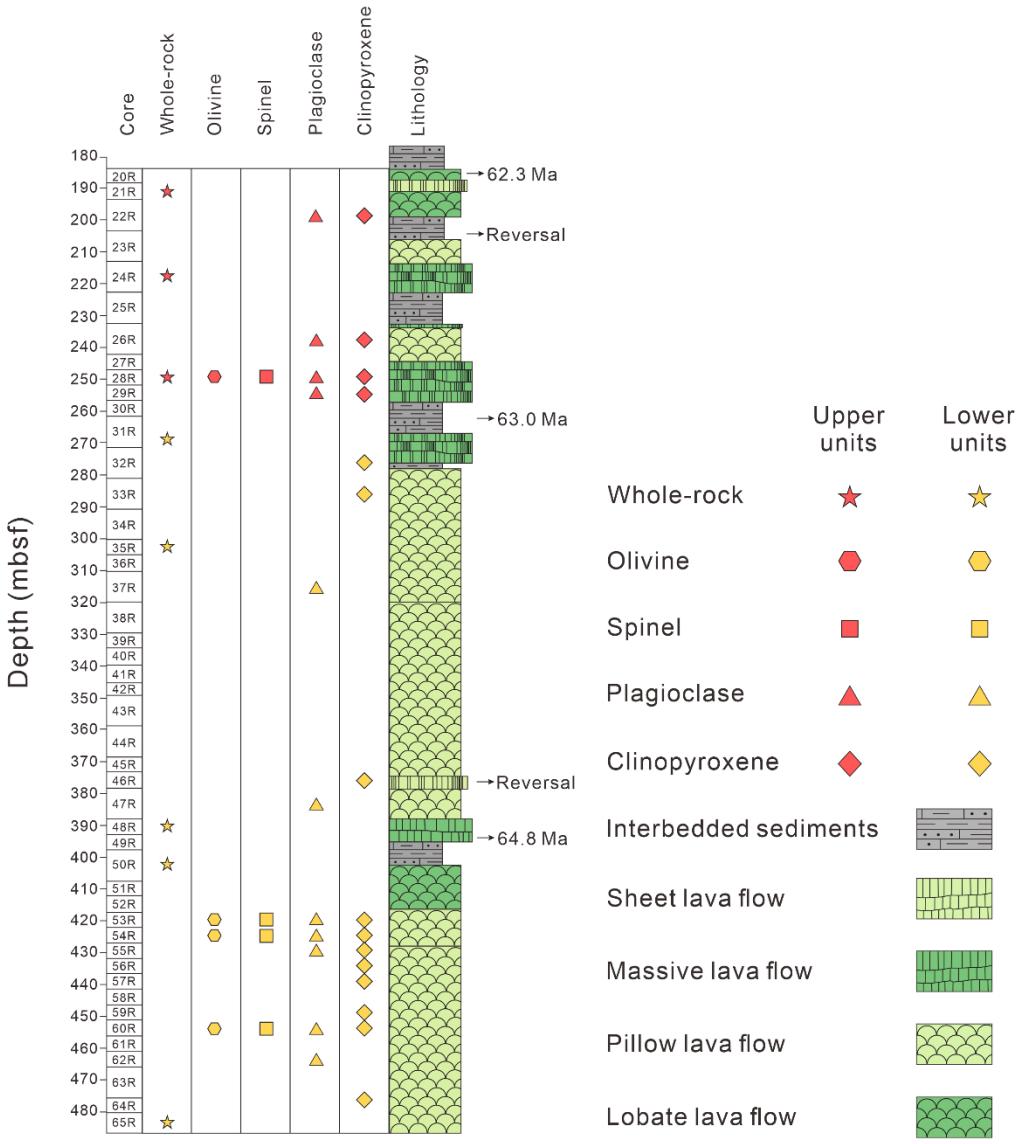

Fig. 2 Lithology of Site U1578 at Walvis Ridge, showing both interbedded sediments and igneous units (Sager and Hoernle, 2022). Site U1578 penetrated 302.14 m of the igneous basement, and it represents the deepest basement penetration established during Expedition 391 and 397T. The igneous units comprise pillow and lobate flows, sheet flows, and massive flows with interbedded sediments. The age estimates and position of magnetic reversals are based on the Expedition 391 preliminary report (Sager and Hoernle, 2022). The star, hexagon, square, triangle, and diamond represent the whole-rock, Ol, Sp, Pl, and Cpx in this study. Mbsf, meters below the sea floor.

https://doi.org/10.1130/B38890.1

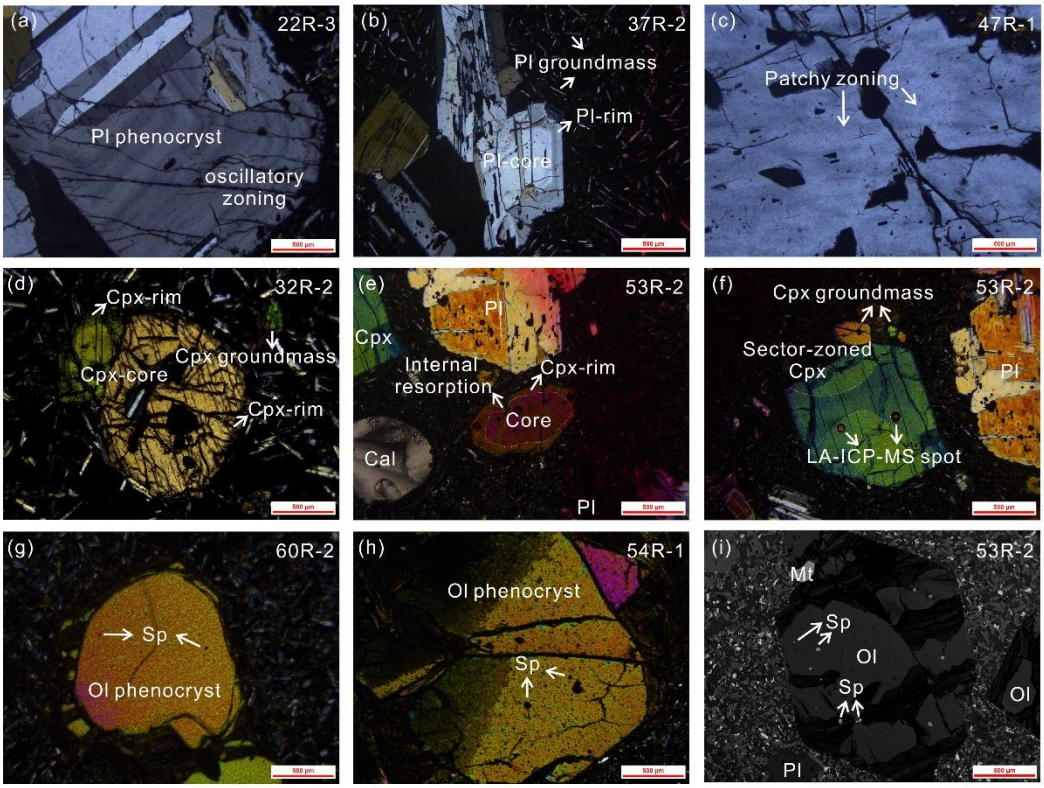

Fig. 3 Cross-polarized light and BSE images of Walvis Ridge volcanic rocks from Site 1578. Zoned Pl phenocrysts under cross-polarized light: (a) oscillatory texture; (b) normal zoning texture; (c) patchy texture. Zoned Cpx phenocrysts under cross-polarized light: (d) normal zoning texture; (e) reverse zoning texture; (f) sector zoning texture. Petrography of large Ol phenocrysts containing abundant euhedral Sp inclusions (g-h: microscopic photo; i: BSE image). Clinopyroxene (Cpx), plagioclase (Pl), olivine (Ol), spinel (Sp), calcite (Cal), magnetite (Mt).

https://doi.org/10.1130/B38890.1

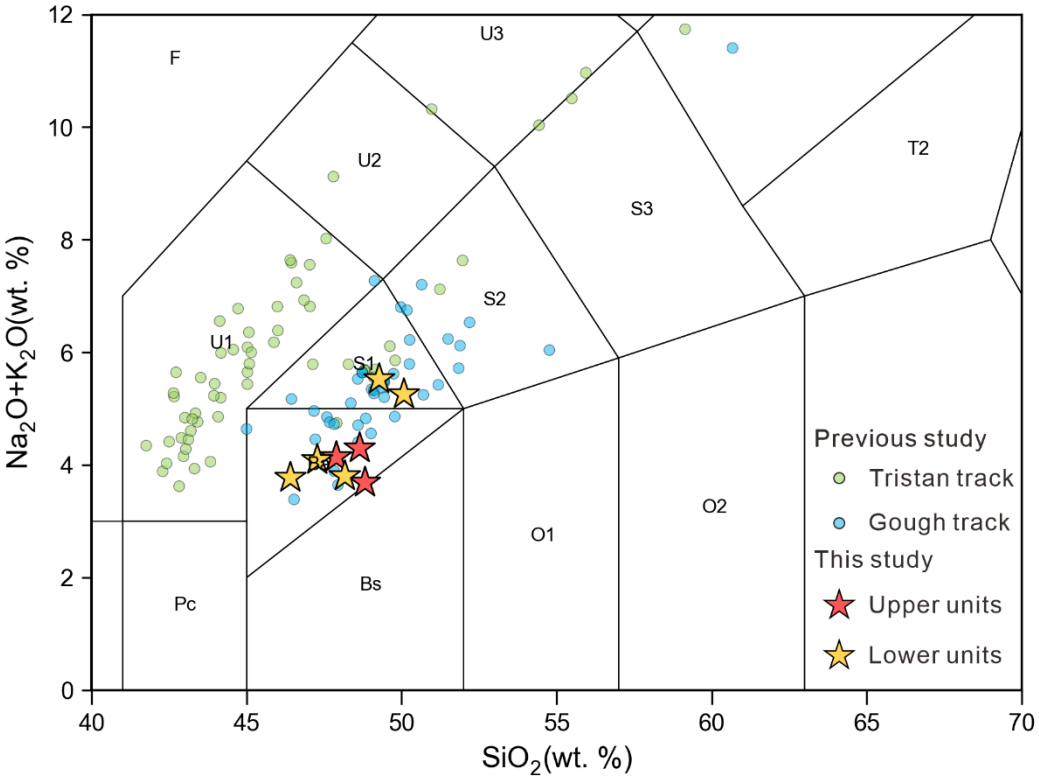

1156

1157 Fig. 4 Total alkalis vs silica (TAS) diagram for volcanic rocks at Site 1578 compared

1158 with other volcanic rocks from Tristan track and Gough track. The red and yellow stars

1159 represent the samples from upper and lower units, respectively.

https://doi.org/10.1130/B38890.1

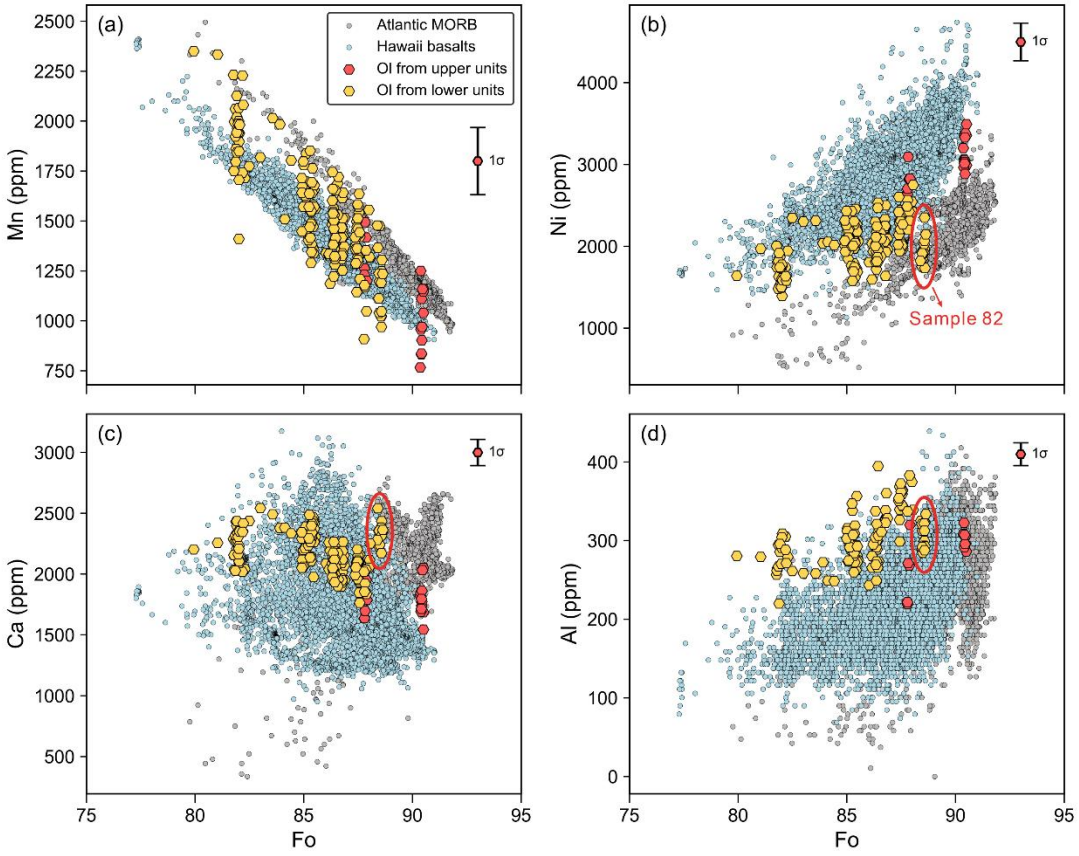

Fig. 5 Olivine Fo content vs Mn (a), Ni (b), Ca (c), and Al (d) concentration in Ol (ppm). The red and yellow hexagons represent the Ol from upper and lower igneous units, respectively (see Fig.2). The grey and blue points represent the Ol from Atlantic MORB and Hawaii basalts, respectively. Representative one standard deviation analytical uncertainties are shown as black bars.

https://doi.org/10.1130/B38890.1

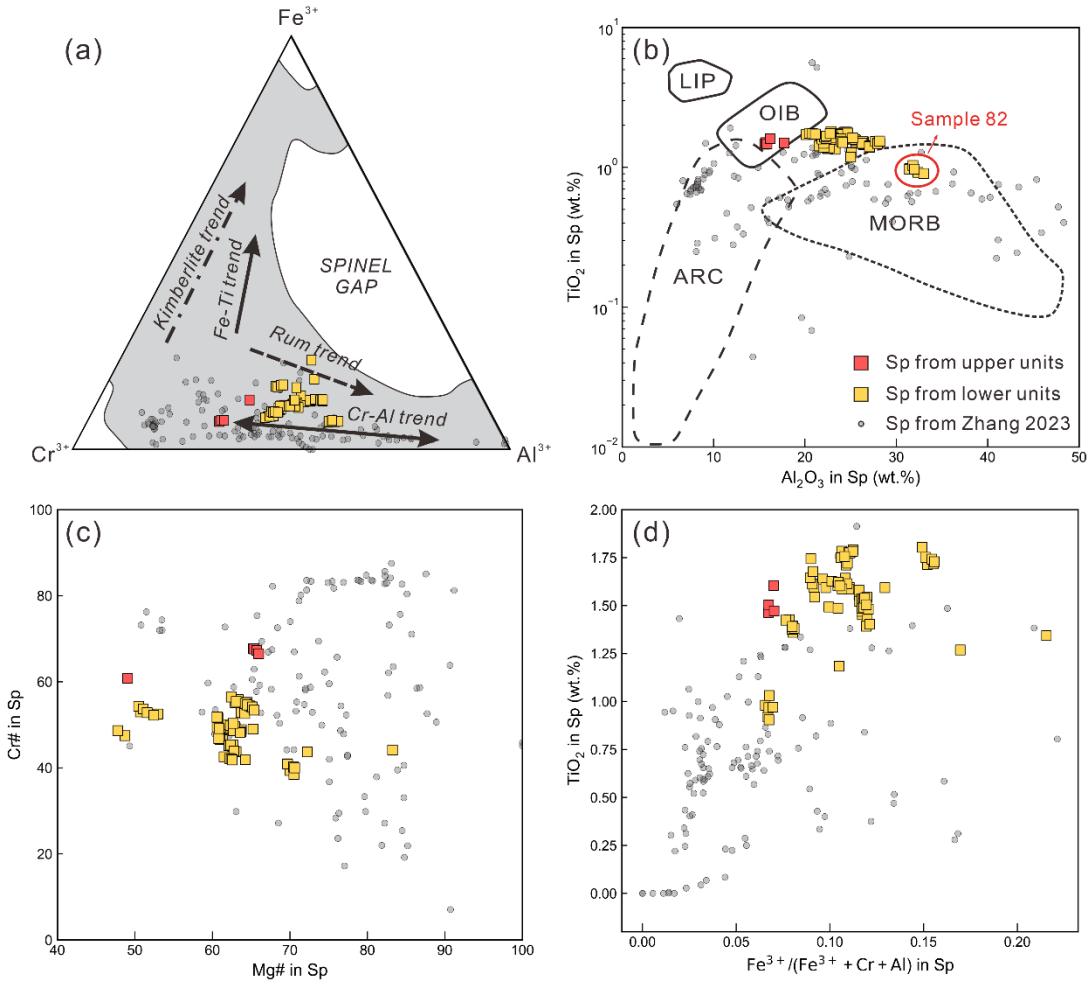

1166

1167 Fig. 6 The compositional variation diagram for Sp. (a) Cr^{3+}-Al^{3+}-Fe^{3+} triangular
1168 diagram for distinguishing the evolution trend of Sp (after Barnes and Roeder, 2001);
1169 (b) Diagram of TiO_2 versus Al_2O_3 for the affinity of Sp to the tectonic settings (after
1170 Kamenetsky et al., 2001); (c) Diagram of Cr# in Sp versus Mg# in Sp; (d) Diagram of
1171 TiO_2 in Sp versus $Fe^{3+}/(Fe^{3+} + Cr + Al)$ in Sp. The red and yellow squares represent the
1172 Sp from upper and lower igneous units, respectively. The grey points represent the Sp
1173 from Zhang et al. (2023) used to calibrate the Al-in-Ol thermometer.

https://doi.org/10.1130/B38890.1

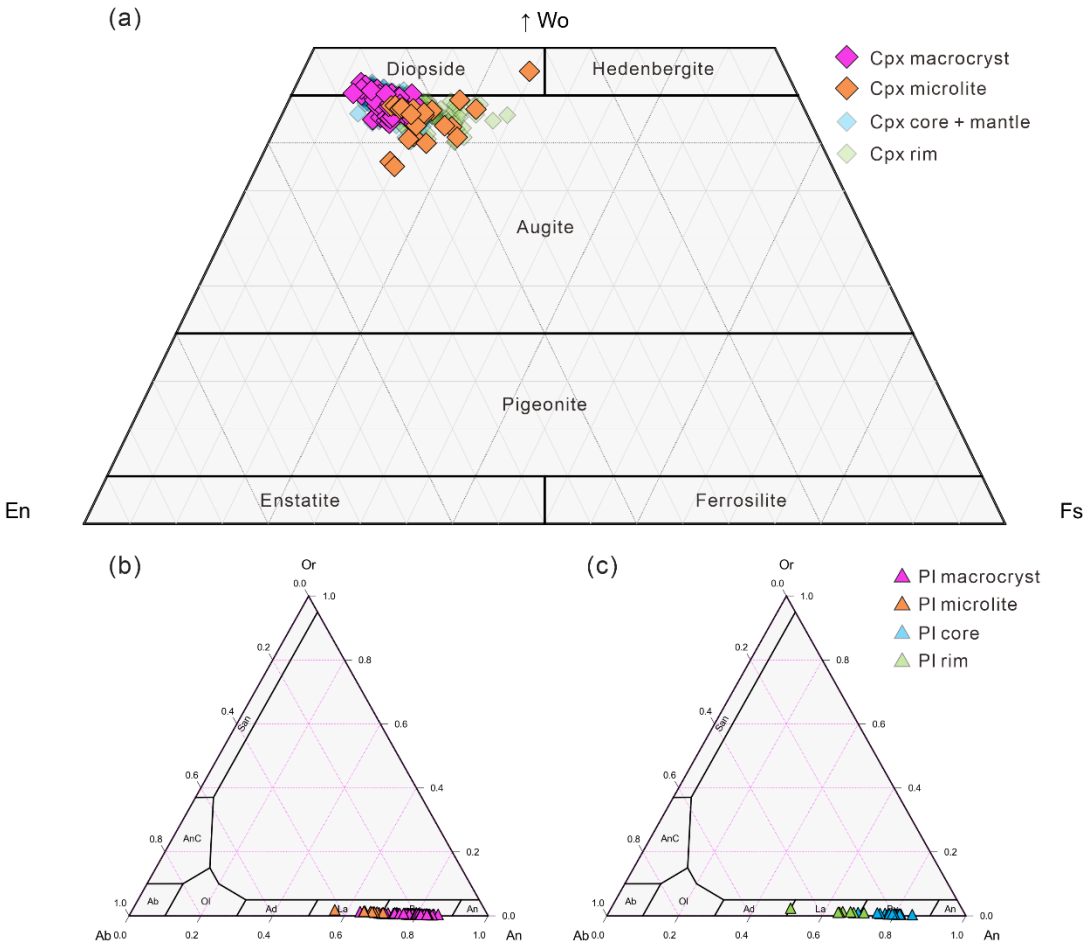

Fig. 7 Compositions of Cpx and Pl from the basaltic lavas cored at Site U1578, Walvis Ridge. The data points are individual measurements obtained for each crystal, plotted in the enstatite-ferrosilite-wollastonite (En-Fs-Wo) ternary diagrams ((a); Morimoto et al., 1988), and the anorthite-albite-orthoclase (An-Ab-Or) ternary diagrams (b and c), which is based on the ternary plot python package (Harper et al., 2015; Wieser et al., 2022). Note that "mantle" in (a) refers to the optically distinguishable area between core and rim for zoned Cpx.

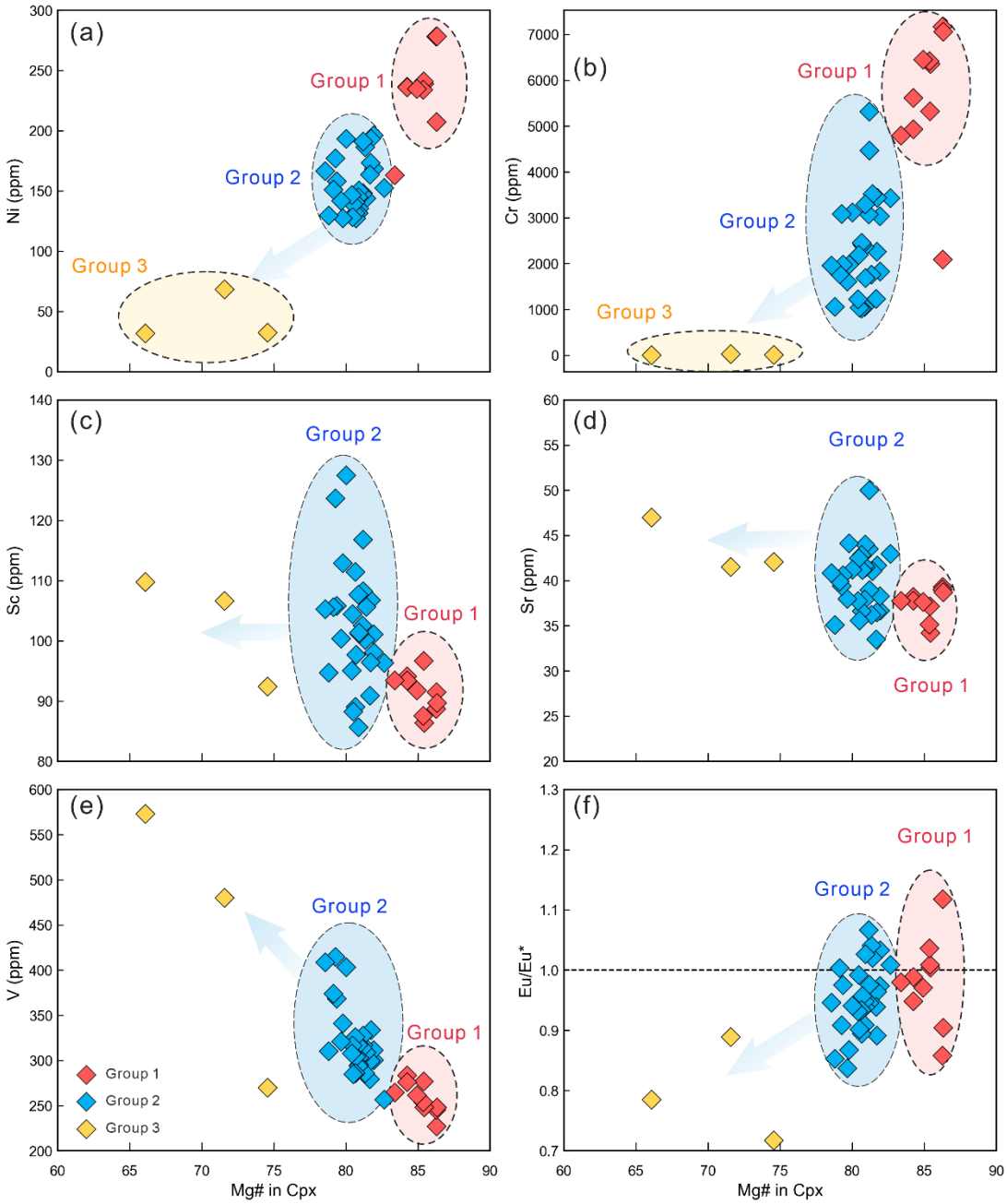

Fig. 8 Plots of Ni (a), Cr (b), Sc (c), Sr (d), V (e), and Eu/Eu* (f) versus Mg# in Cpx. The horizontal dashed line in (f) represents whether the Cpx shows Eu anomalies ($Eu/Eu^* = Eu_N/ (Sm_N \times Gd_N)0.5$). The blue trend lines represent the variations of trace elements during the fractionation history. The red, blue, and yellow diamonds represent the Cpx from Group 1, Group 2 and Group 3, respectively.

https://doi.org/10.1130/B38890.1

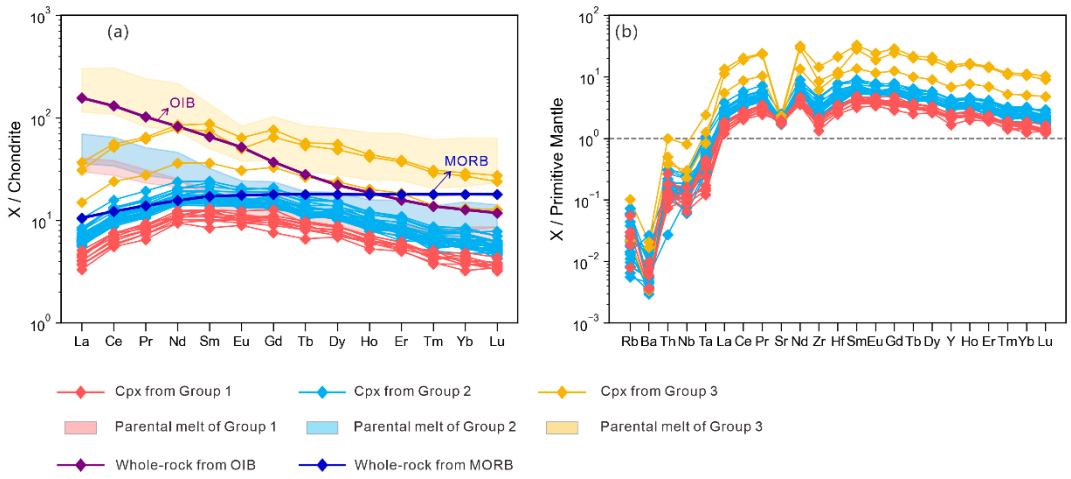

Fig. 9 Chondrites-normalized REE diagrams (a) and primitive mantle-normalized trace element abundances diagrams (b) for Cpx in this study. All the data used here were acquired by LA-ICP-MS. The red, blue, and yellow areas in (a) show REE patterns for hypothetical melts in equilibrium with Cpx from Group 1, Group 2, and Group 3 respectively, calculated using partition coefficients ($K_D(Fe\text{-}Mg)^{Cpx\text{-}melt}$) from Sun and Liang (2012). OIB, MORB data and chondrite values are from Sun and McDonough (1989). Primitive mantle normalization values are from McDonough and Sun (1995). This figure is based on the REE plot python package (Williams et al., 2020).

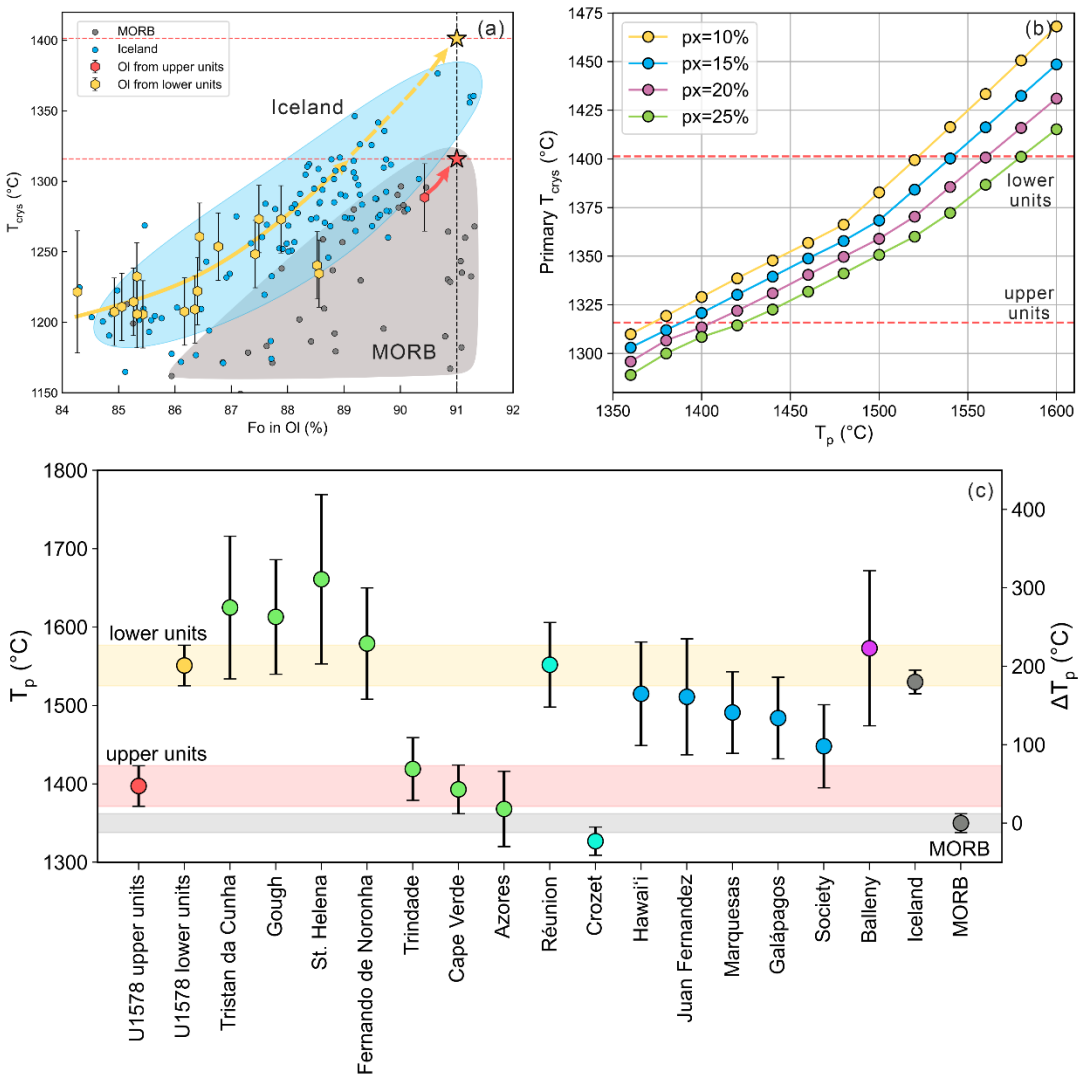

Fig. 10 (a) Al-in-Ol crystallization temperatures vs. Ol Fo content for Site U1578, Walvis Ridge in comparison with those for Iceland (Matthews et al., 2016; Spice et al., 2016) and MORB (Coogan et al., 2014; Matthews et al., 2021). The yellow and red curves show the result of extrapolating a liquid line of descent from the crystallization temperature and Ol composition to Fo_{91} Ol from lower and upper units. (b) pyMELT simulation results showing primary crystallization temperatures calculated by inputting different mantle potential temperatures at four possible source pyroxenite fractions (px = 10%, 15%, 20%, and 25%). (c) Comparison of mantle potential temperatures from the Center track with those of mid-ocean ridge basalts, Icelandic basalts, and global

ocean island basalts (Li et al., 2025). The error bars on Tp were estimated by propagating the errors from the Ol thermometer and from extrapolating the liquid line of descent used to calculate the primary crystallization temperature.

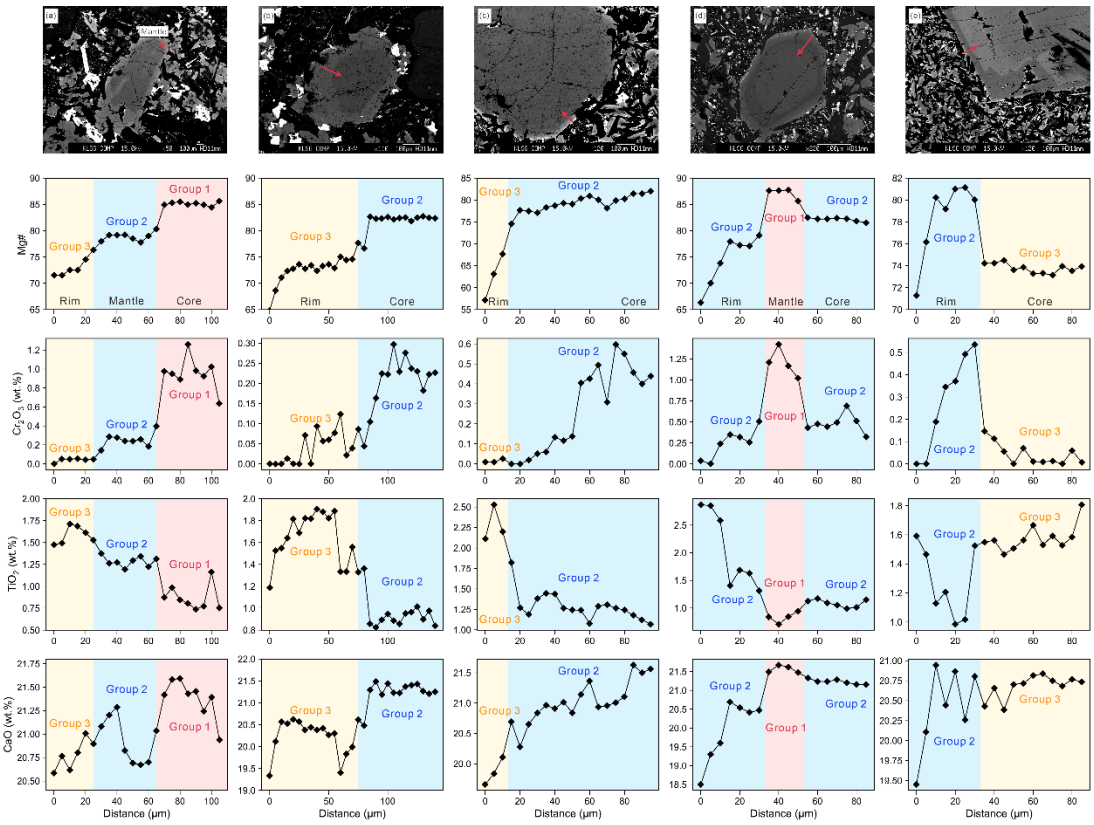

Fig. 11 Representative BSE images and analytical points with major element compositions for zoned Cpx from volcanic rocks at Site 1578, Walvis Ridge. (a-c) are normal zoned Cpx and (d-e) are reverse zoned Cpx. The red arrows represent the location of the electron microprobe traverses across the zoning. The red, blue, and yellow areas represent the Cpx from Group 1, Group 2 and Group 3, respectively.

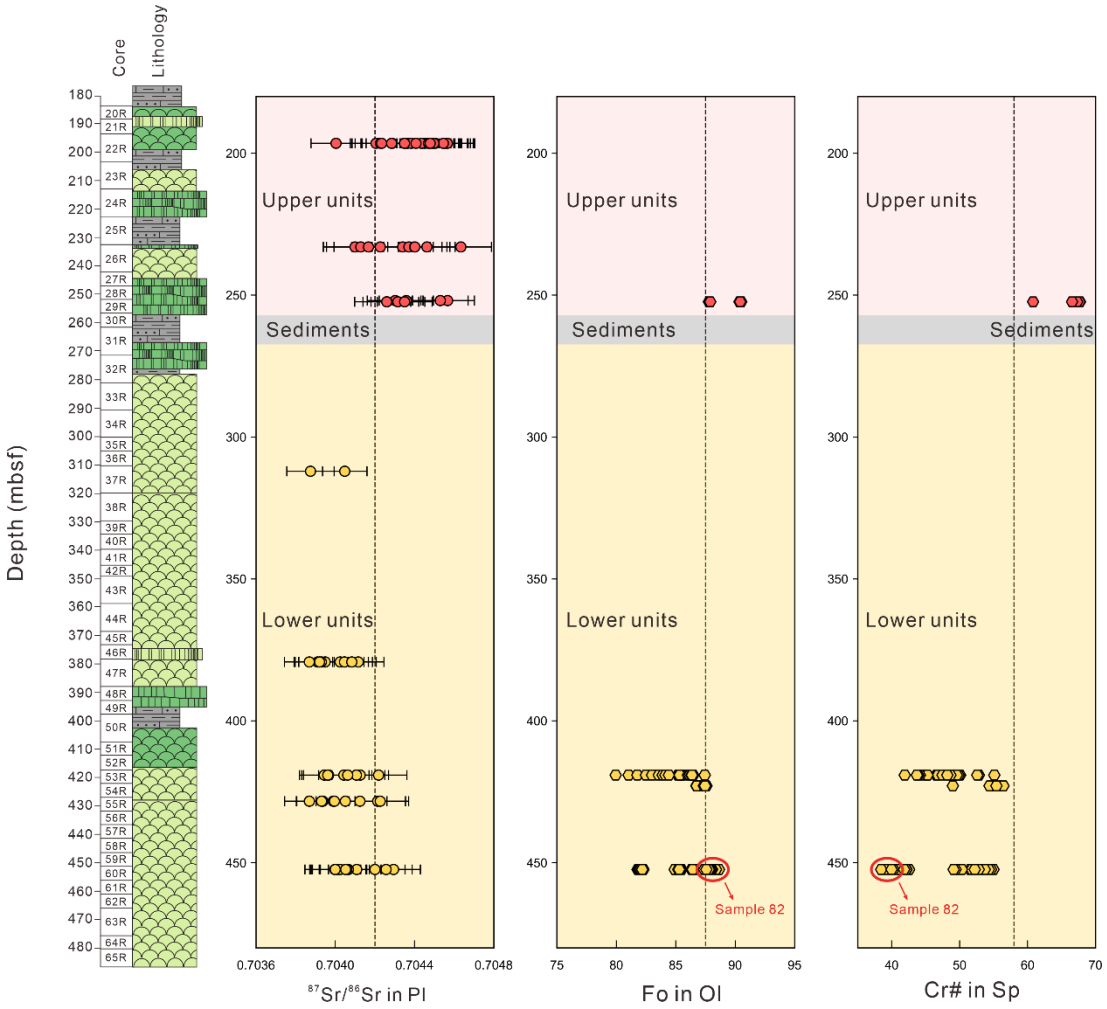

Fig. 12 Downhole chemical variations in Sr isotopes in Pl, Fo in Ol, and Cr# in Sp. The red and yellow circles/hexagons represent the Pl/Ol from the upper and lower igneous units of Site U1578, respectively. The red, grey, and yellow areas on the stratigraphic column represent the upper igneous units, sediments, and lower igneous units, respectively.

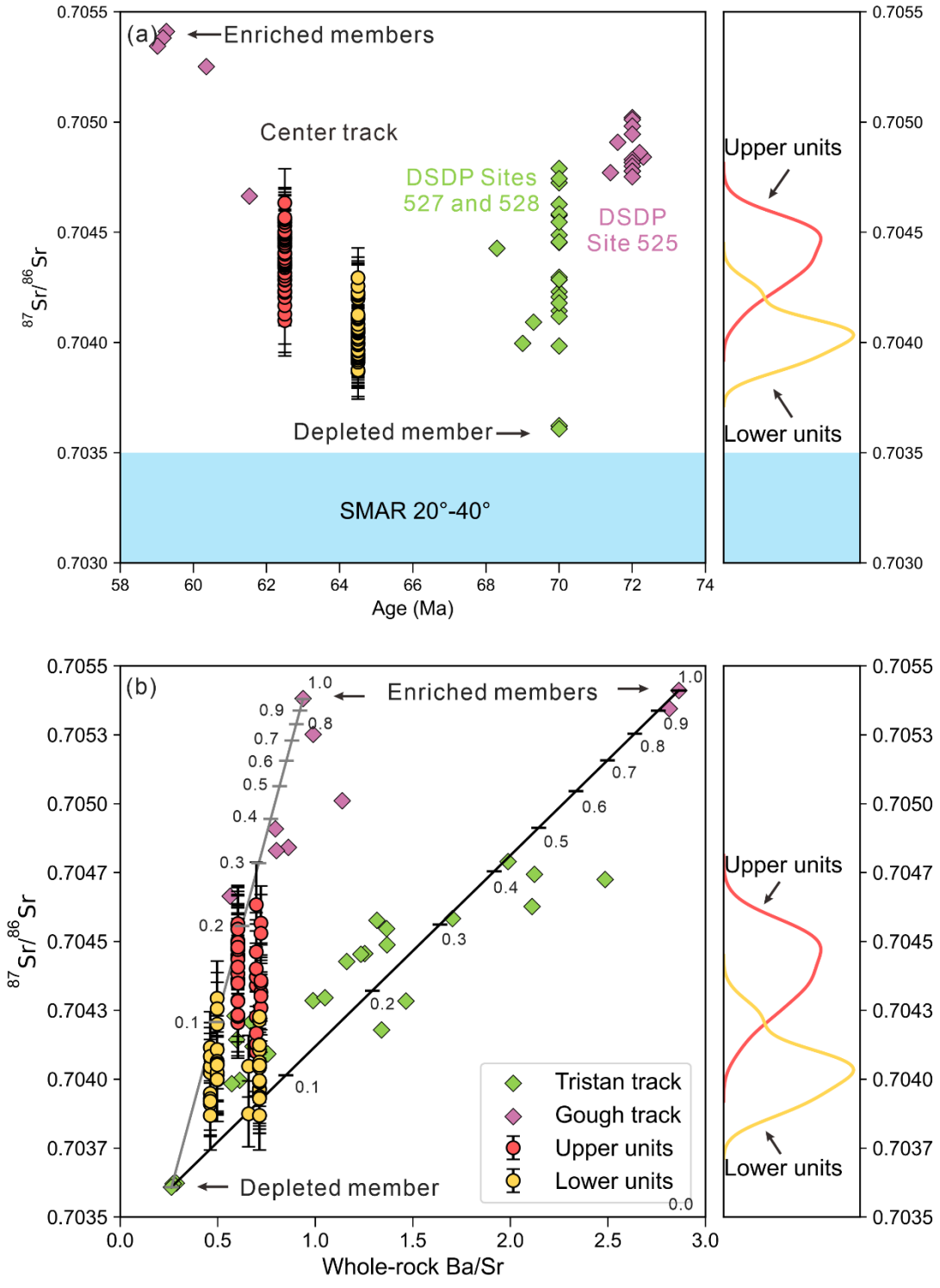

1224

1225 Fig. 13 (a) Ages for each sample versus $^{87}Sr/^{86}Sr$ ratios from the Center track, Tristan

1226 track, and Gough track. The red and yellow circles represent the Pl from the upper and

1227 lower igneous units of Site U1578, respectively. The green and purple diamonds

represent the literature whole-rock data from the Tristan and Gough tracks (Hoernle et al., 2015; Homrighausen et al., 2019; Rohde et al., 2013a; Rohde et al., 2013b; Salters and Sachi-Kocher, 2010). Sample locations for these analyses are shown on Fig.1. (b) Binary mixing model of whole-rock Sr isotope ratios versus Ba/Sr concentration, with the KDE curves on the right showing the distribution of Center track Sr isotope ratios of Pl.

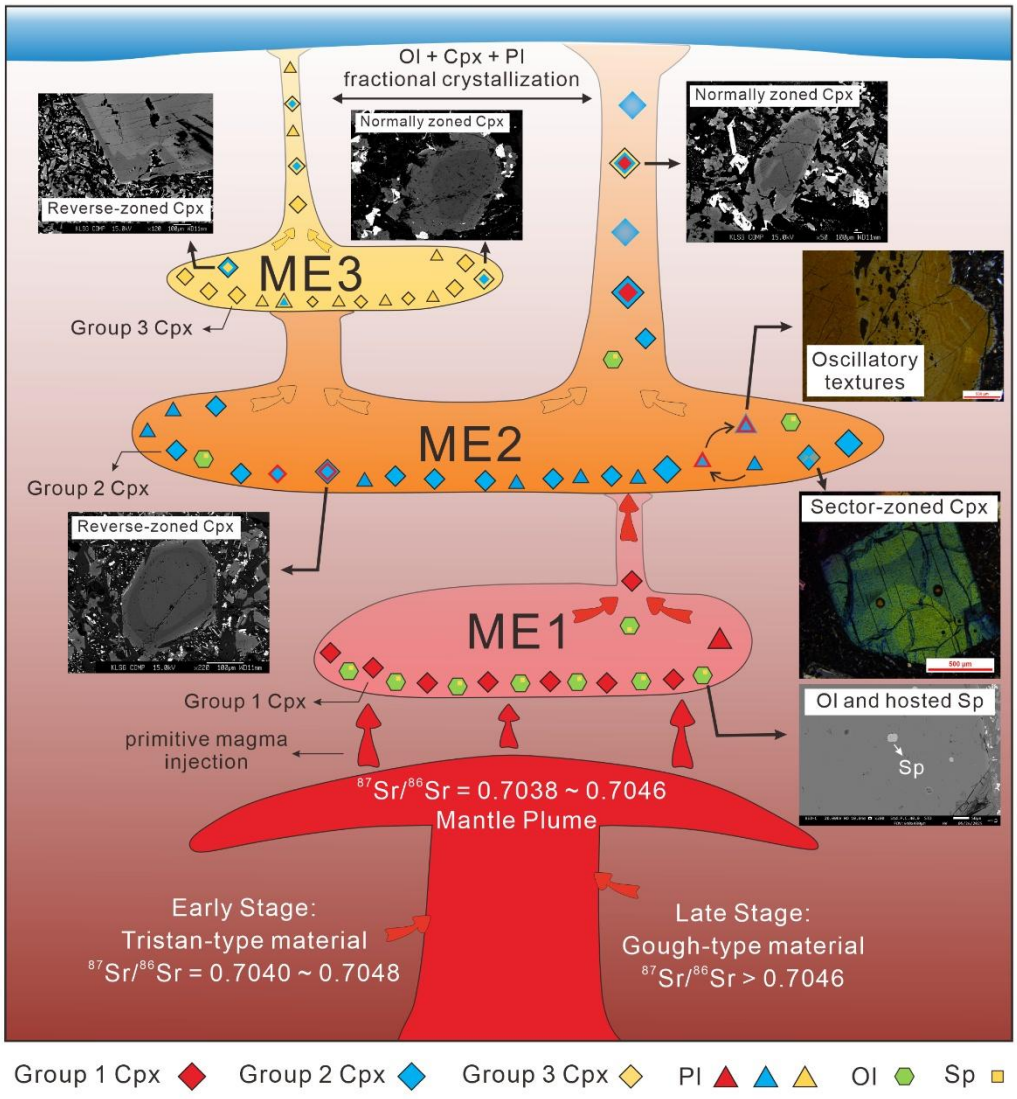

Fig. 14 A petrologic model for the magmatic plumbing system of the Center track in Walvis Ridge according to in-situ major, trace elements and Sr isotopes of Ol, Cpx, and

Pl from IODP Site U1578 in this study. Depths and connections between reservoirs are largely schematic, and reservoirs may be separated vertically, horizontally, or both.

Table 1 The average compositions of Ol, Sp and Pl from Site U1578 upper units, lower units and Sample 82. – available upon request

Table 2 The average compositions of Group 1, 2 and 3 Cpx from Site U1578. – available upon request

https://doi.org/10.1130/B38890.1

Supplementary Text S1. Ol-Sp thermometry and Monte Carlo error propagation

Prior to temperature calculations, we ensure equilibrium conditions between Ol and Sp by conducting high-resolution compositional transects (~2 μm spacing) across each Ol-Sp pair. Equilibrium is assessed based on established Fe^{3+}/Fe^{2+} and Cr–Al-Mg partitioning behavior (Coogan et al., 2014; Zhang et al., 2023). Olivine and spinel are generally euhedral, also suggesting they formed at equilibrium. Data points used for thermometry, indicated by grey bars in Fig.S3, are averaged and subsequently used for temperature calculations. This profiling approach avoids the influence of secondary fluorescence (Matthews et al., 2016), thereby yielding more robust and representative results.

Temperatures are calculated using the Ol-Sp equilibrium thermometry equations provided by Zhang et al. (2023), and the results are reported in Table S2A. The thermometric calibration spans a wide range of P–T–composition conditions (1174–1606 °C, 0.1–1350 MPa, up to 7.4 wt.% H_2O) and encompasses the compositional range of Sp from most OIB samples, including our dataset (Fig.6). We apply equations 5 and 7 of Zhang et al. (2023) and use a statistical Z-test, following the method outlined in their study, to determine the most appropriate crystallization temperature for each Ol-Sp pair. Using the same method, we also calculate crystallization temperatures for Ol-Sp pairs from other OIBs (Li et al., 2025; Matthews et al., 2021), MORBs (Coogan et al., 2014; Matthews et al., 2021), and Iceland samples (Matthews et al., 2016; Spice et al., 2016) to compare, and all results are reported in Tables S2B-D.

To quantify uncertainty, we apply Monte Carlo error propagation for four representative Ol-Sp pairs from Center track. Each Monte Carlo simulation is repeated 1,000 times, generating a distribution of temperature estimates from which the mean and standard deviation were calculated.

By employing a high beam current (150 nA) and extended counting times, the analytical uncertainty (1σ) for Al in Ol was reduced to ~17 ppm. Using the Python script of Zhang et al. (2023), we propagated the analytical uncertainties of all elements measured in Ol and Sp (Table S1B), and the results show that the propagated uncertainty in temperature estimates ranges from 5.6 to 10.8 °C (Table S2E). According to Zhang et al. (2023), the uncertainty on the Ol-Sp Al-exchange thermometer from experimental calibration is ± 23.9 °C. Therefore, the combined uncertainty — calculated as $\sigma_{overall} = \sqrt{(\sigma^2_{equation} + \sigma^2_{analysis})}$ — is only slightly (0–2 °C) higher than the calibration uncertainty alone. These results demonstrate that analytical uncertainties associated with EDS-WDS measurements have a limited impact on the calculated temperature values.

https://doi.org/10.1130/B38890.1

Supplementary Text S2. Cpx-melt and Cpx-only thermobarometry

In order to understand the chemical and structural evolution of magmatic plumbing system further, pressures and temperatures are estimated by clinopyroxene-only (Cpx-only) and clinopyroxene-melt (Cpx-melt) thermobarometry by using the open-source Python3 package Thermobar v. 1.0.41 (Wieser et al., 2022). Cpx-only thermobarometry is from Jorgenson et al. (2022), and Cpx-melt barometry and thermometry are from Neave and Putirka (2017) and Putirka (2008, eq. 33). All calculated results are shown in Tables S3A and B. Note that crystals with strong sector zoning are excluded from our calculation (MacDonald et al., 2023; Ubide et al., 2019).

For the Cpx-melt thermobarometry, we use the major element data for the Center track volcanic rocks from different core sections of Site U1578 (Fig.2; Table S3A) as the liquid compositions and liquid compositions are matched with every Cpx composition in Thermobar. We then use thresholds of 0.06, 0.05, and 0.03 for the DiHd, EnFs, and CaTs (DiHd: diopside + hedenbergite, CaTs: Ca-Tschermak, and EnFs: enstatite + ferrosilite) components respectively (Mollo et al., 2013; Putirka, 1999) to filter the disequilibrium data (Fig.S6). This study performs the calculation using the total amount of Fe (Fe_{tot}) in the Cpx and liquid. Considering N=553 Cpx and N=8 Liquid, there are a total of N=4424 Liq-Cpx pairs. Finally, the Cpx-Liquid melt matching algorithm finds a total of N=618 Cpx-Liq matches by using the specified filter and N=397 Cpx match to one or more liquids (Table S3A). Then we plot N=397 Cpx-Liq pairs on a Rhodes diagram and each liquid composition is the average of all equilibrium liquids for one Cpx. Nearly all values fall within the fields using a $K_D^{Cpx\text{-}Liq}$ of 0.28±0.08 (Putirka, 2008). For P-T estimates, we use only Cpx-liquid pairs that passed the applied equilibrium tests and apply the Cpx-melt thermometer presented in Putirka (2008) (eq. 33, SEE = ±45 °C) and Cpx-melt barometer presented in Neave and Putirka (2017) (SEE = ±140

MPa). All calculated results are shown in Table S3A and Fig.S7a.

Clinopyroxene-only thermobarometry is also one of the most practical tools to reconstruct crystallization pressures and temperatures of Cpx, and it does not require any information of coexisting silicate melt. Thus, P-T conditions of N=553 Cpx are all calculated by the machine learning-based Cpx thermobarometry (Jorgenson et al., 2022) (SEE = ±320 MPa and ±51 °C) using the open-source Python3 package Thermobar v. 1.0.41 (Wieser et al., 2022). All calculated results are shown in Table S3B and Fig.S7b. We also try the calculations for other different existing thermobarometry models: the Cpx-melt barometer (eq. 30, SEE = ±160 MPa) of Putirka (2008) and the thermometer (eq. 33, SEE = ±45 °C) of Putirka (2008) (Table S3C); the Cpx-melt barometer (SEE =± 260 MPa) and thermometer (SEE = ±40.0 °C) of Petrelli et al. (2020) (Table S3D); the Cpx-melt barometer (SEE =± 270 MPa) and thermometer (SEE = ±44.9 °C) of Jorgenson, C. et al. (2020) (Table S3E); and the Cpx-only barometer (eq. 1, SEE = ±166 MPa) and thermometer (eq. 2, SEE = ±36.6 °C) of Wang, X. et al. (2021) (Table S3F). These models are chosen because they are the most appropriate for alkali magma compositions from Site U1578.

For Group 1 Cpx crystals, the Mg# values of their equilibrium melt are much higher than their host rocks (Fig.S6d), thus we could not find an appropriate melt composition to calculate their P–T conditions when using Cpx-melt thermobarometry. P–T crystallization conditions obtained from Group 2 and 3 Cpx-melt pairs show that they have similar pressures and temperatures with different Mg# contents, suggesting they crystallized in separate magma reservoirs at the same depth (Fig.S7a). Based on Cpx-only thermobarometry (Jorgenson et al., 2022), Group 1 Cpx may have originated from relatively deeper and hotter magmatic environments, which could be interpreted as antecrysts crystallized in primitive magma and subsequently captured by evolved magma (Chen et al., 2018;

Li et al., 2020). However, when considering the uncertainties associated with thermobarometry, we argue that it is not possible to clearly resolve two independent magma reservoirs at different depths beneath the Center track. Taken together, the entire plumbing system depth can be constrained to 0 -20 km (assuming an average crustal density of 2850 kg/m^3 following Huang and Li (2024)) and EPMA analytical uncertainties have a minimal effect on P-T estimation based on the Monte Carlo error propagation results (Supplementary Text S3; Table S4), which do not significantly impact our interpretation. Combined with seismological evidence for a Moho depth of about 12 km (Geissler et al., 2017; Huang and Li, 2024), our results suggest that the entire plumbing system is located within the crust and uppermost mantle near the Moho (Fig.S7), which is consistent with observations from Tristan da Cunha Island (Weit et al., 2017).

Supplementary Text S3. Monte Carlo error propagation for Cpx thermobarometry

Recent studies have highlighted that Cpx barometers can be sensitive to analytical uncertainties inherent in electron probe microanalysis (EPMA) of mineral compositions (Wieser et al., 2023; Wieser et al., 2024). To assess the impact of such uncertainties on calculated temperatures and pressures in this study, we conduct Monte Carlo error propagation using the open-source Python3 package Thermobar v.1.0.41 (Wieser et al., 2022).

We employ the *add_noise_sample_1phase* function in Thermobar to generate synthetic datasets for both mineral and melt compositions. These datasets simulate analytical uncertainty by creating normally distributed compositions around each measured value. The 1σ percentage errors are estimated from repeated EPMA analyses of Cpx and repeated XRF analyses of associated melt phases. For each valid Cpx-Liq pair, 1000 synthetic compositions were generated. For example, N = 397 equilibrium Cpx-Liq pairs passed our filtering criteria, resulting in N = 397,000 synthetic pairs used for thermobarometric calculations. The results of Monte Carlo error simulation (Fig.S8) are summarized below.

Cpx-melt thermobarometer: ~95% of the propagated temperature uncertainties ($1\sigma_{analysis}$) fall within ±10 °C (Fig. S8a and Table. S4A), and pressure uncertainties within ±100 MPa (Fig. S8b and Table. S4B). The uncertainty of the Cpx-melt thermometer ($1\sigma_{equation}$) presented in Putirka (2008) (eq. 33) and barometer presented in Neave and Putirka (2017) are ±45 °C and ±140 MPa. The overall errors calculate from combining errors on the thermobarometer equations and the analyses, using $\sigma_{overall} = \sqrt{(\sigma^2_{equation} + \sigma^2_{analysis})}$, is only slightly (0–1.2°C, 0-32 MPa) higher than errors induced by the thermobarometer equations alone.

Cpx-only thermobarometer: ~95% of propagated temperature uncertainties are within ±30 °C

(Fig. S8c and Table. S4C), and pressure uncertainties within ±70 MPa (Fig. S8d and Table. S4D). The uncertainty of the Cpx-melt thermometer and barometer presented in Jorgenson et al., (2022) are ±51 °C and ±320 MPa. The overall errors calculate from combining errors on the thermobarometer equations and the analyses, using $\sigma_{overall} = \sqrt{(\sigma^2_{equation} + \sigma^2_{analysis})}$, is only slightly (0–8.2 °C, 0-8 MPa) higher than errors induced by the thermobarometer equations alone.

These results demonstrate that the analytical uncertainties associated with EPMA have a limited impact on the calculated P–T values. Therefore, they do not significantly influence our thermobarometric interpretations.

Supplementary Figure S1

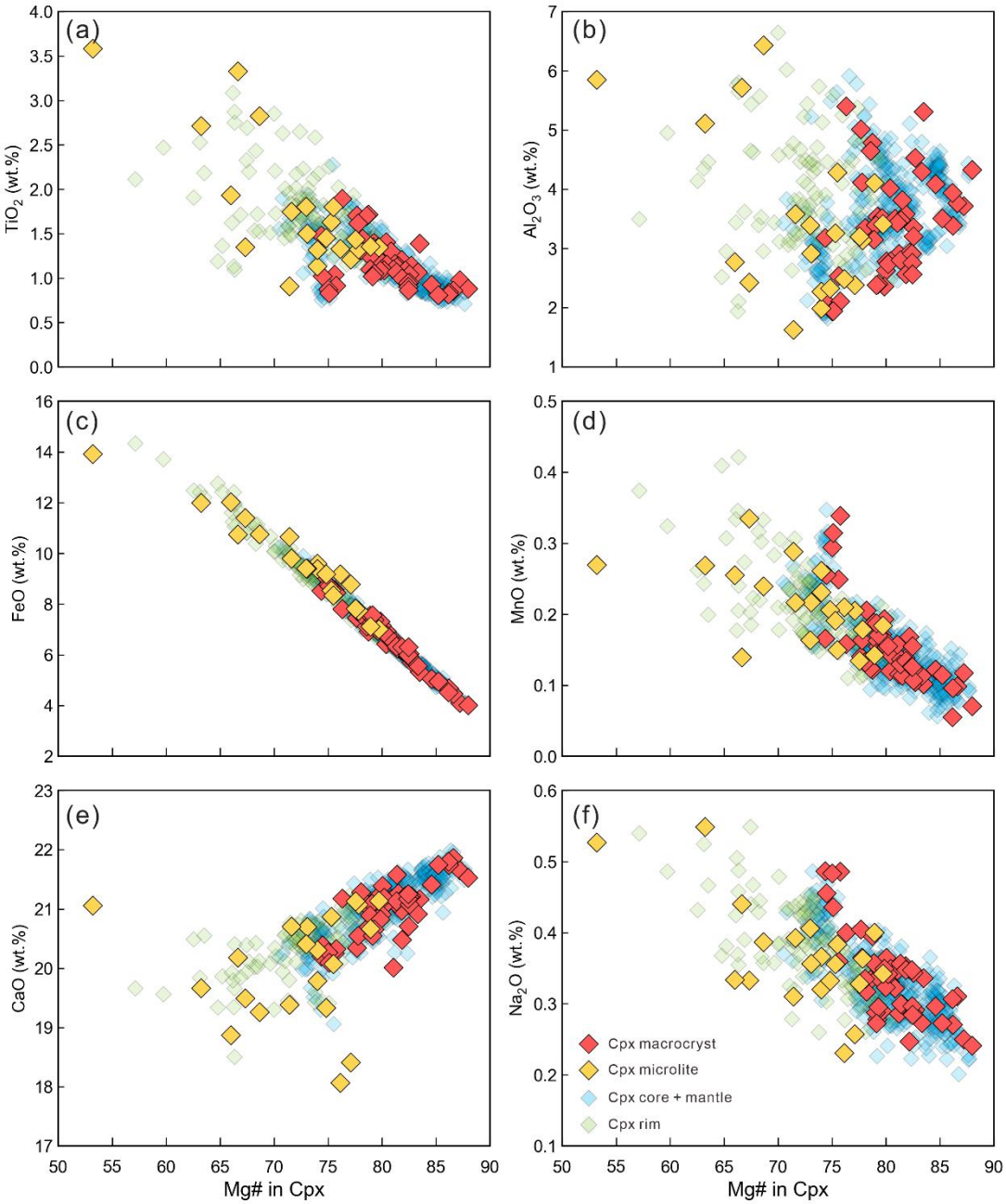

Fig. S1 Plots of TiO_2 (a), Al_2O_3 (b), FeO (c), MnO (d), CaO (e), and Na_2O (f) versus Mg# in Cpx.

All the data used here were acquired by EPMA.

https://doi.org/10.1130/B38890.1

Supplementary Figure S2

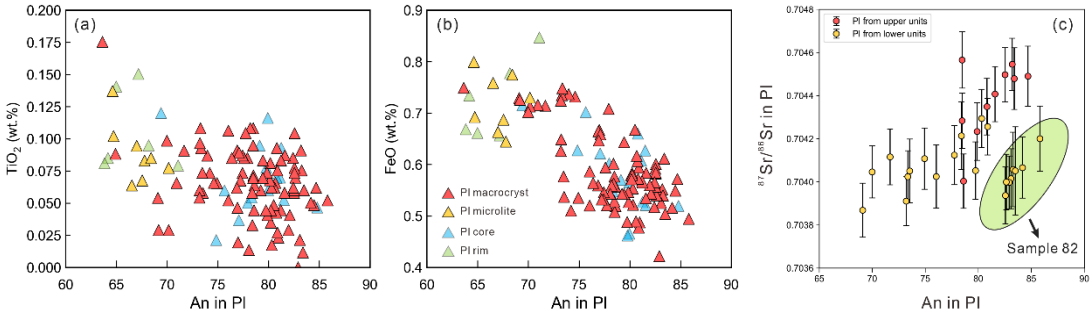

Fig. S2 Compositions of Pl macrocrysts and microlites from the basaltic lavas cored at Site U1578, Walvis Ridge. Plots of TiO2 (a), FeO (b) and Sr isotope (c) versus An (%) in Pl.

https://doi.org/10.1130/B38890.1

Supplementary Figure S3

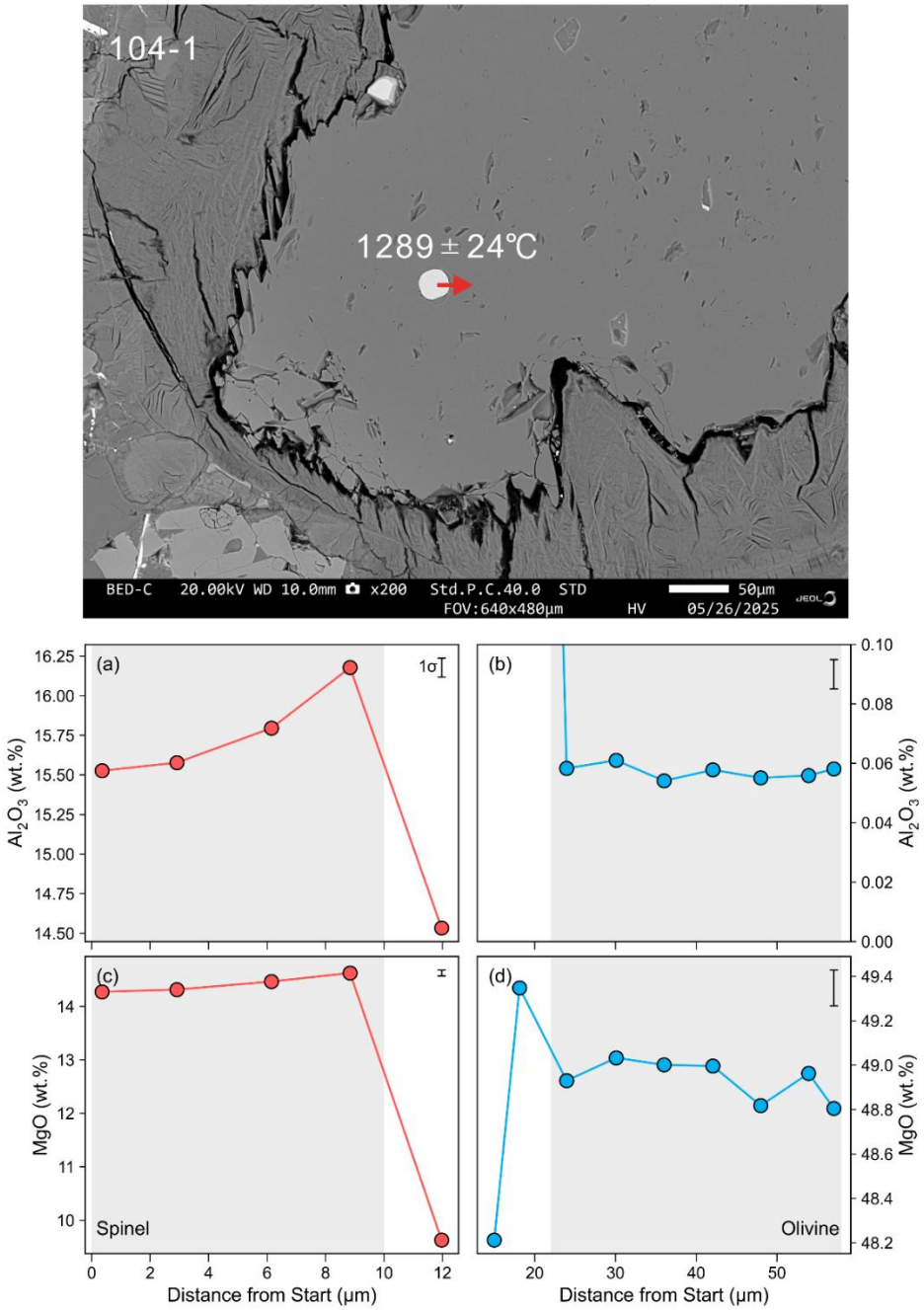

Fig. S3 Backscatter Electron Image for Center track Ol crystal 104-1. A profile was measured by SEM-EDS-WDS through both Sp and Ol as shown the red arrow. The grey bars indicate points included in the thermometry calculations. Representative one standard deviation analytical uncertainties are shown as black bars. The temperature calculated for this profile and its uncertainty are shown on the BSE image.

https://doi.org/10.1130/B38890.1

Supplementary Figure S4

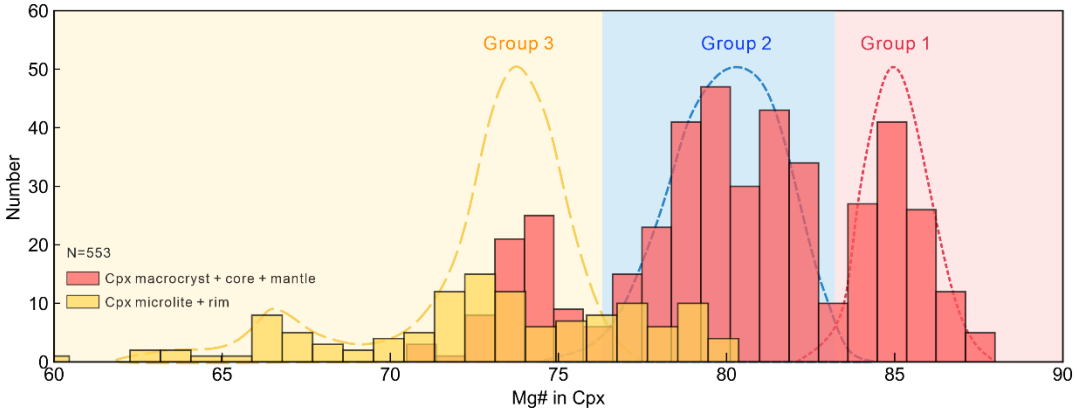

Fig. S4 Distribution of Mg# contents of Cpx macrocrysts and microlites from the basaltic lavas cored at Site U1578, Walvis Ridge. The red, blue, and yellow areas represent the range of Mg# in Cpx from Group 1, Group 2 and Group 3, respectively.

https://doi.org/10.1130/B38890.1

Supplementary Figure S5

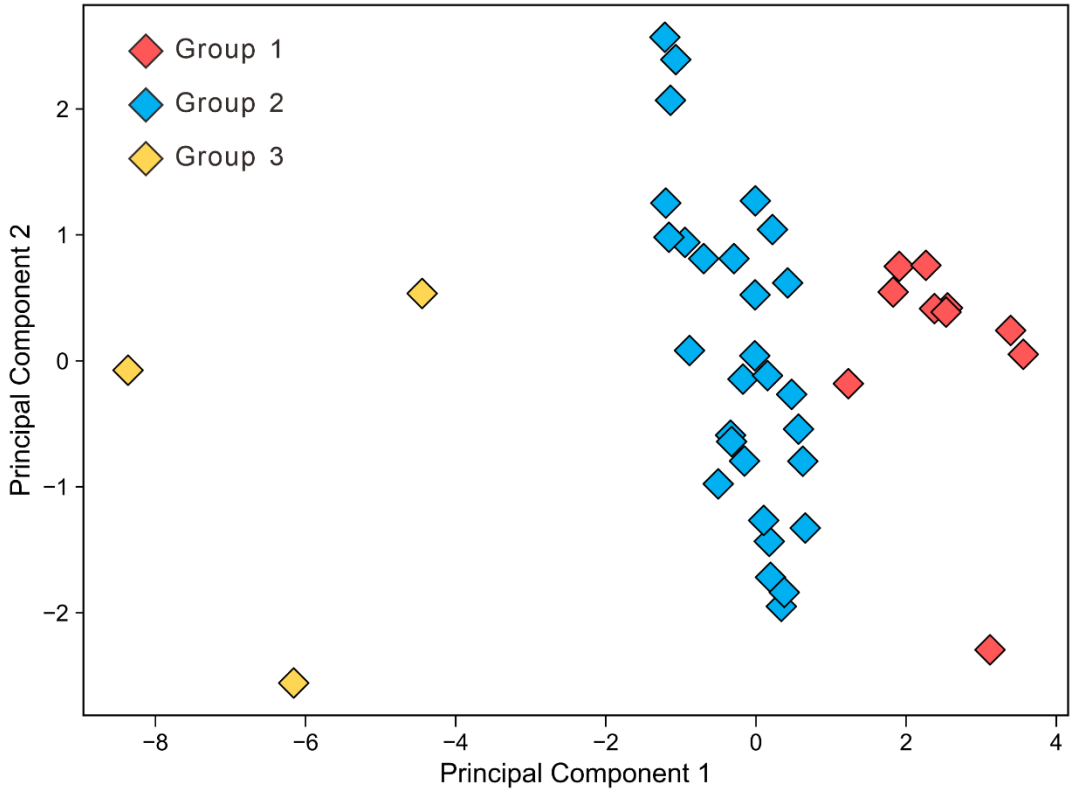

Fig. S5 K-means cluster analysis of Cpx based on eight geochemical parameters: Mg#, Na_2O, Sc, Cr, Ni, La, Y and jadeite content of Cpx. The red, blue, and yellow diamonds represent the Cpx from Group 1, Group 2 and Group 3, respectively.

https://doi.org/10.1130/B38890.1

Supplementary Figure S6

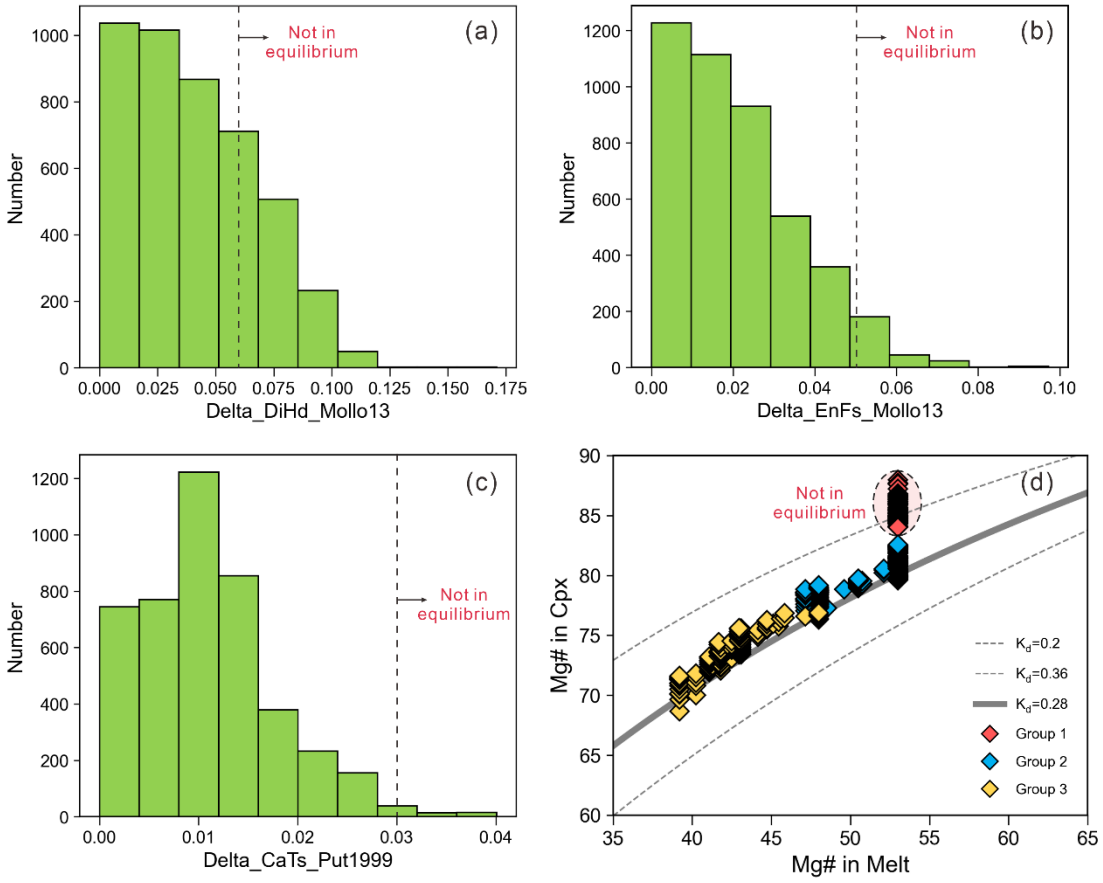

Fig. S6 The Cpx-melt equilibrium test. The tests were carried out by calculating the measured DiHd (a), EnFs (b), and CaTs (c) values. We use thresholds of 0.06, 0.05, and 0.03 for the DiHd, EnFs, and CaTs components respectively to filter the disequilibrium data (Mollo et al., 2013; Putirka, 1999; Putirka, 2008).The Cpx and whole-rock values are plotted in the Rhodes diagram to illustrate this equilibrium test (Rhodes et al., 1979). The grey and dashed lines define the equilibrium curves between Cpx and melt (d), which were calculated using $K_D(Fe\text{-}Mg)^{Cpx\text{-}melt} = 0.28 \pm 0.08$ (Putirka, 2008). The red, blue, and yellow diamonds represent the Cpx from Group 1, Group 2 and Group 3, respectively.

https://doi.org/10.1130/B38890.1

Supplementary Figure S7

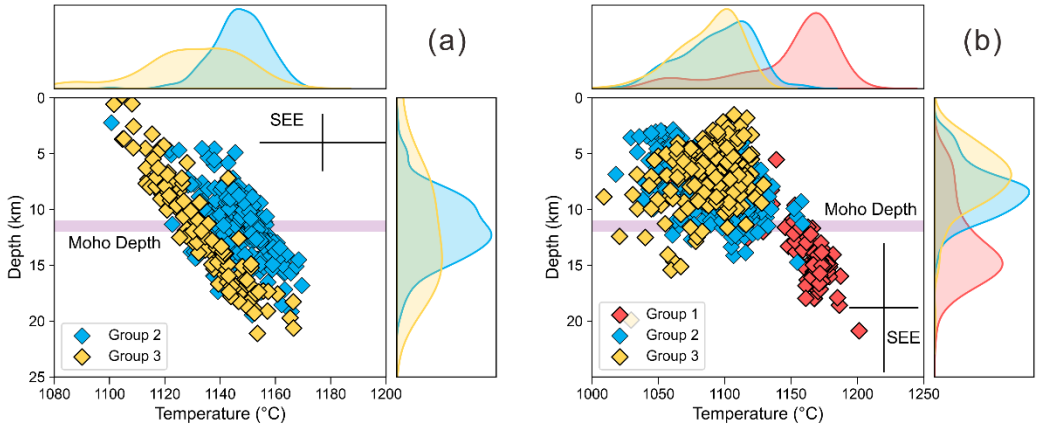

Fig. S7 Plots of crystallization depth versus temperature of Group 1, 2, 3 Cpx. The red, blue, and yellow diamonds represent the Cpx from Group 1, Group 2 and Group 3, respectively. (a) Cpx-melt thermobarometry (Neave and Putirka, 2017; Putirka, 2008); (b) Cpx-only thermobarometry (Jorgenson et al., 2022). The depth of Moho is about 12 km according to the seismological evidence (Geissler et al., 2017; Huang and Li, 2024).

https://doi.org/10.1130/B38890.1

Supplementary Figure S8

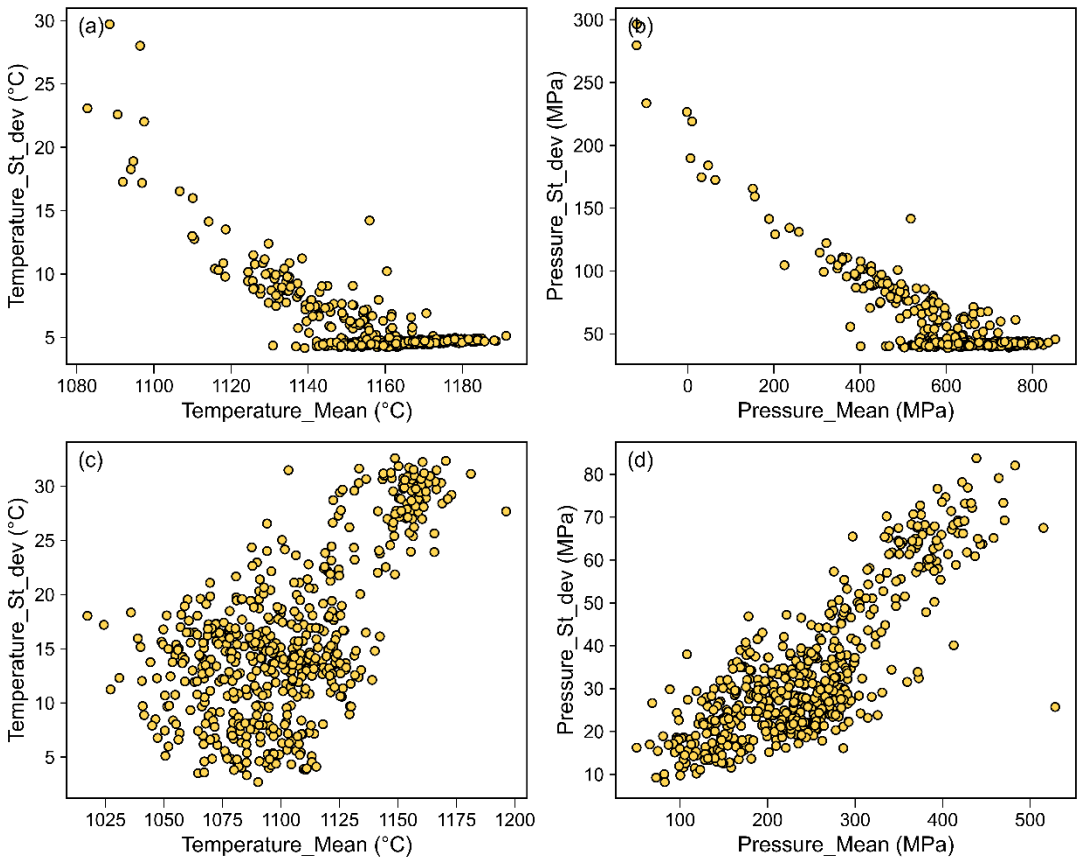

Fig. S8 Monte Carlo error propagation results for Cpx thermobarometry. Panels (a) and (b) show temperature and pressure uncertainties for the Cpx–melt thermobarometer, with ~95% of propagated temperature errors within ±10 °C and pressure errors within ±100 MPa. Panels (c) and (d) display uncertainties for the Cpx-only thermobarometer, with ~95% of temperature errors within ±30 °C and pressure errors within ±70 MPa.

https://doi.org/10.1130/B38890.1

Supplementary Figure S9

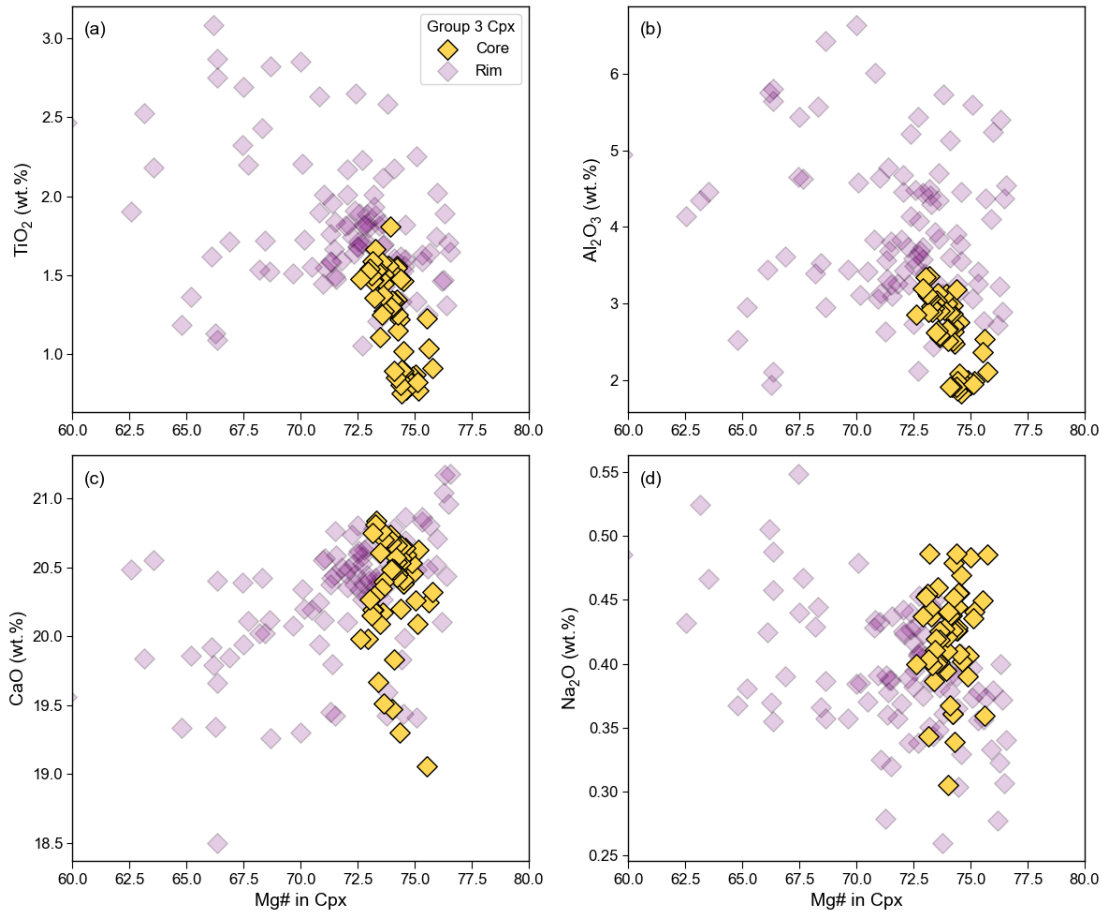

Fig. S9 Plots of TiO2 (a), Al2O3 (b), CaO (c), and Na2O (d) versus Mg# in Group 3 Cpx. All the data used here were acquired by EPMA.

https://doi.org/10.1130/B38890.1

Supplementary Figure S10

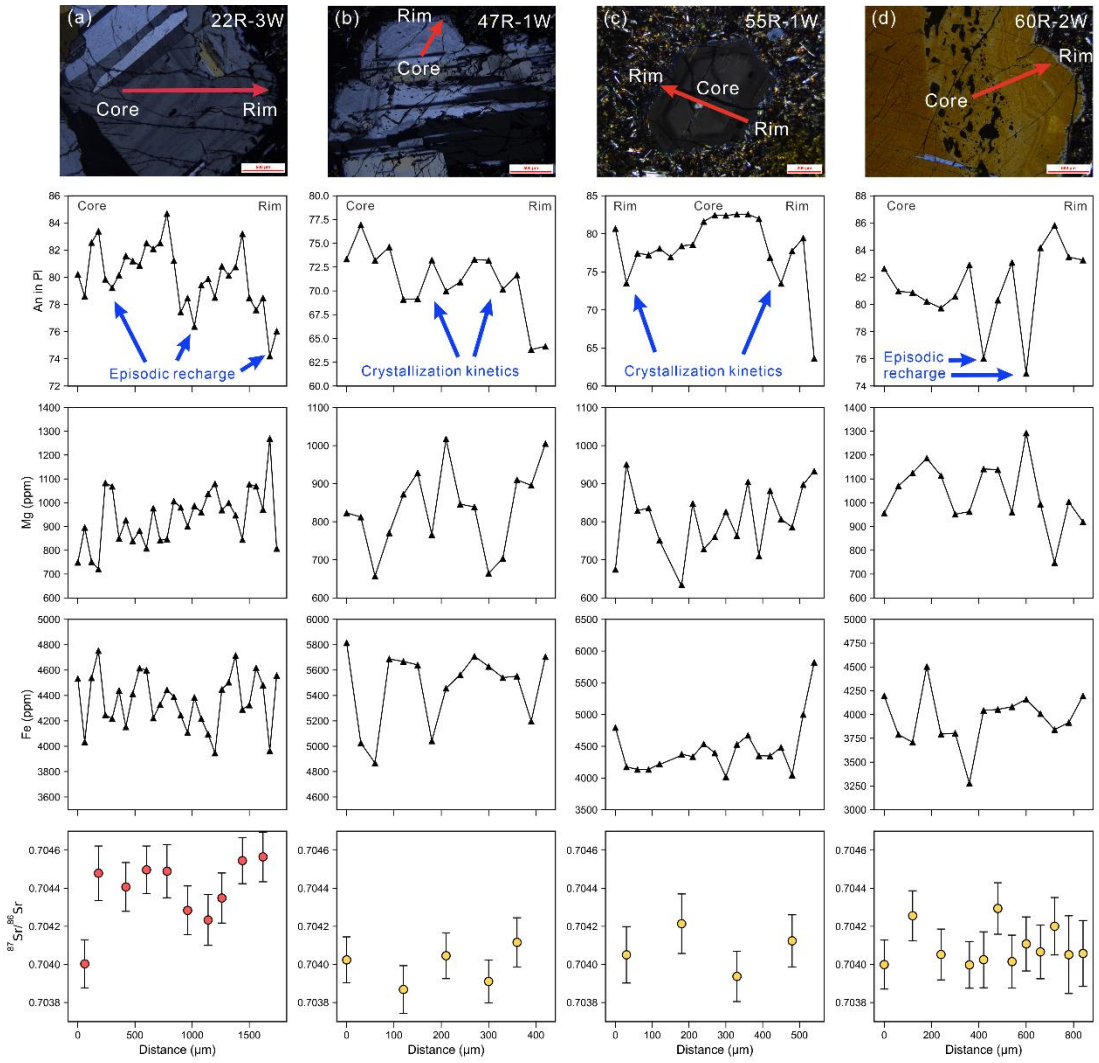

Fig. S10 Representative BSE images and analytical points with major element compositions and Sr isotopes for zoned Pl from volcanic rocks at Site 1578, Walvis Ridge. The red arrows represent the location of the electron microprobe traverses across the zoning.

https://doi.org/10.1130/B38890.1

Supplementary Figure S11

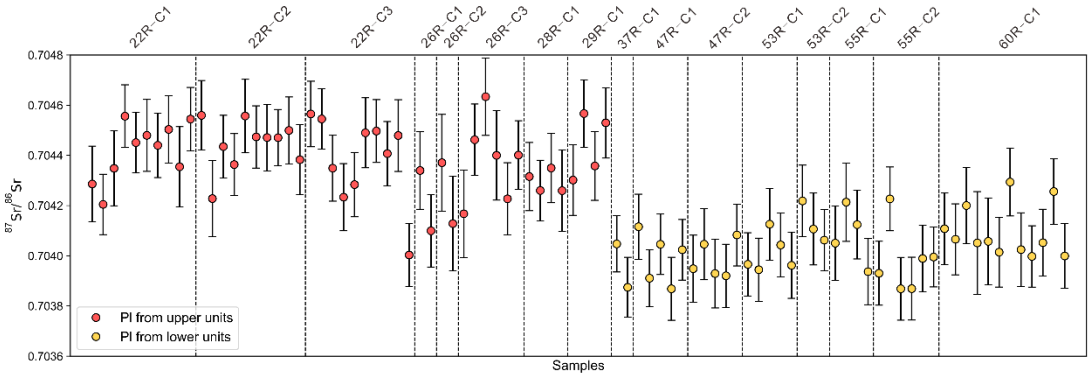

Fig. S11 Sr isotopic compositions and associated uncertainties for Pl phenocrysts from volcanic rocks at Site U1578, Walvis Ridge. Within a single crystal, variations are mostly unresolvable within analytical uncertainty. Sample labels such as "22R-C1" denote the core section (22R) and the first analyzed Pl crystal from that section (C1).

https://doi.org/10.1130/B38890.1

Supplementary Figure S12

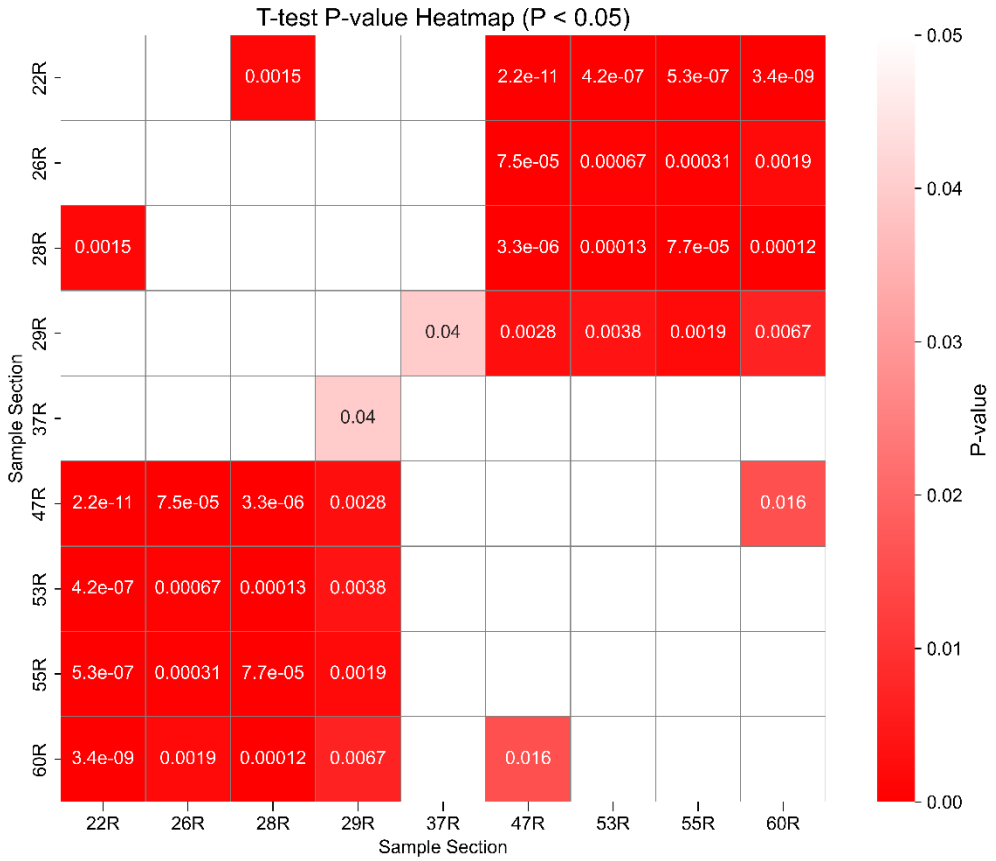

Fig. S12 Heatmap showing statistical differences in $^{87}Sr/^{86}Sr$ values between Pl grains from nine different core sections. The heatmap summarizes the results of two-sample t-tests performed on all 36 pairwise combinations, with numbers indicating p-values less than 0.05 that highlight statistically significant differences. Detailed t-test results, including t-statistics and p-values, are provided in Table S5.

https://doi.org/10.1130/B38890.1

Supplementary Figure S13

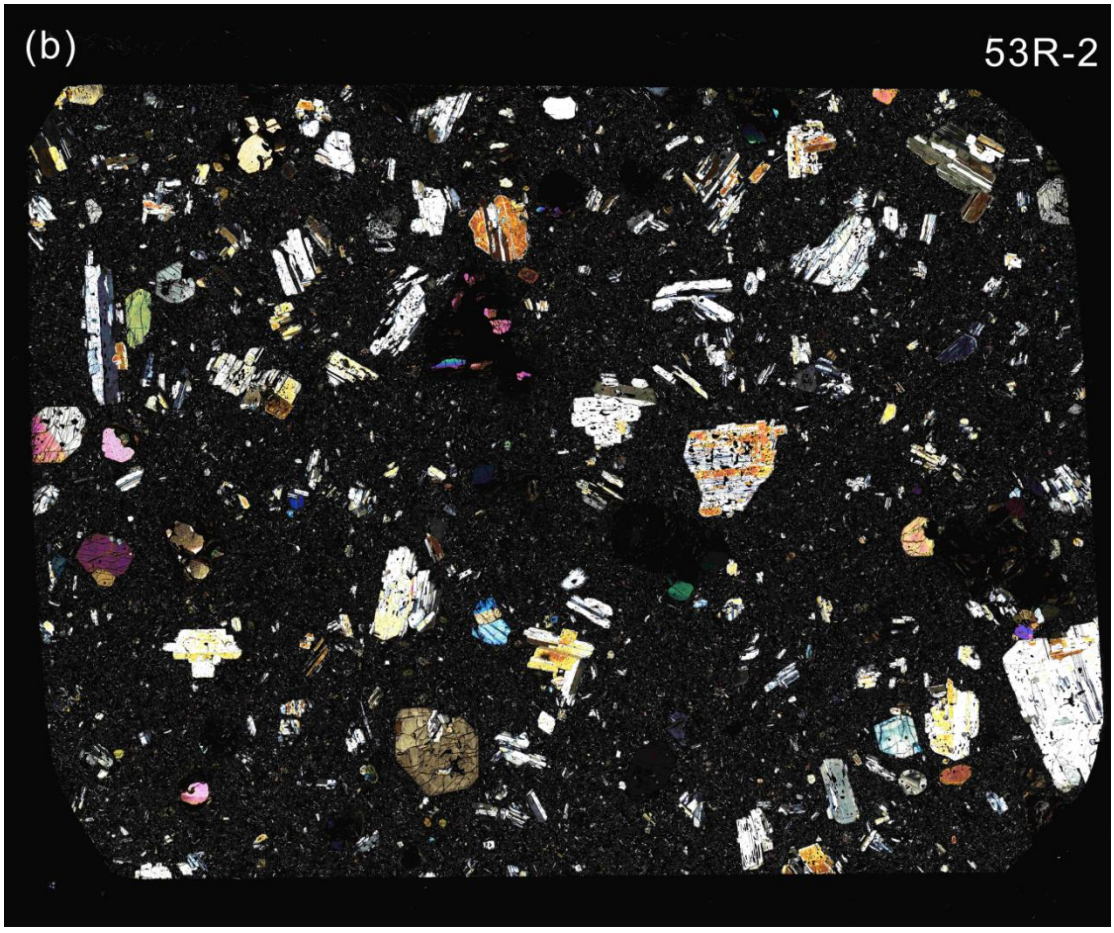

https://doi.org/10.1130/B38890.1

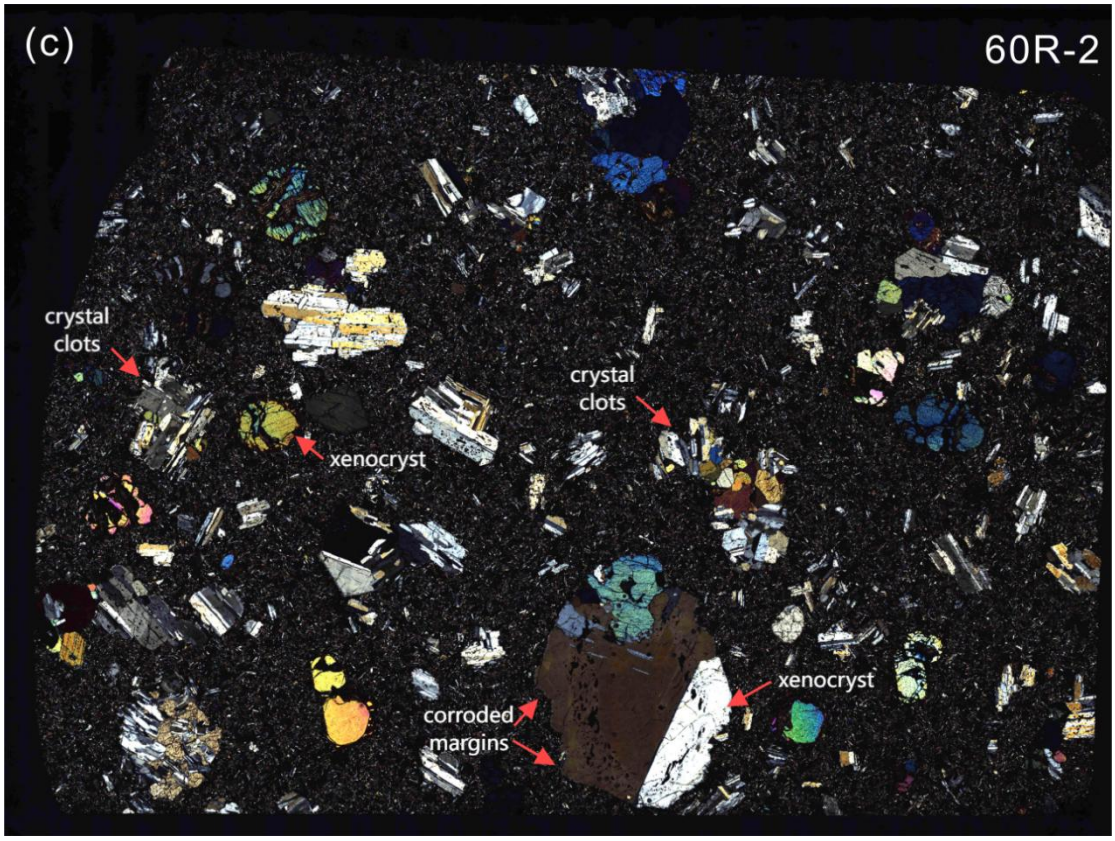

Fig. S13 Cross-polarized light photomicrographs of three thin sections (28R-5 from the upper unit, 53R-2 and 60R-2 from the lower unit) demonstrating fresh Pl and Cpx phenocrysts with sharp crystal boundaries, absence of alteration rims, and no secondary overgrowths or pseudomorphs. Whole thin section scans made using a WITec alpha300R Raman microscope with a motorized stage.

References (supplementary materials):

Chen, L., Zheng, Y. and Zhao, Z., 2018. Geochemical insights from clinopyroxene phenocrysts into the effect of magmatic processes on petrogenesis of intermediate volcanics. Lithos, 316-317: 137-153.

Coogan, L.A., Saunders, A.D. and Wilson, R.N., 2014. Aluminum-in-olivine thermometry of primitive basalts: Evidence of an anomalously hot mantle source for large igneous provinces. Chemical Geology, 368: 1-10.

Geissler, W.H., Jokat, W., Jegen, M. and Baba, K., 2017. Thickness of the oceanic crust, the lithosphere, and the mantle transition zone in the vicinity of the Tristan da Cunha hot spot estimated from ocean-bottom and ocean-island seismometer receiver functions. Tectonophysics, 716: 33-51.

Harper, M. et al., 2015. python-ternary: Ternary Plots in Python. Zenodo.

Huang, L. and Li, C., 2024. What controls the magma production rate along the Walvis Ridge, South Atlantic? Tectonophysics: 230381.

Jorgenson, C., Higgins, O., Petrelli, M., Bégué, F. and Caricchi, L., 2022. A Machine Learning-Based Approach to Clinopyroxene Thermobarometry: Model Optimization and Distribution for Use in Earth Sciences. Journal of Geophysical Research: Solid Earth, 127(4): e2021JB022904.

Li, W. et al., 2025. Taking the temperature of ocean islands: a petrological approach. Journal of Petrology: egaf033.

Li, X. et al., 2020. Integrated major and trace element study of clinopyroxene in basic, intermediate and acidic volcanic rocks from the middle Okinawa Trough: Insights into petrogenesis and the influence of subduction component. Lithos, 352-353: 105320.

MacDonald, A., Ubide, T., Mollo, S., Pontesilli, A. and Masotta, M., 2023. The Influence of Undercooling and Sector Zoning on Clinopyroxene–Melt Equilibrium and Thermobarometry. Journal of Petrology: egad074.

Matthews, S., Shorttle, O. and Maclennan, J., 2016. The temperature of the Icelandic mantle from olivine-spinel aluminum exchange thermometry. Geochemistry, Geophysics, Geosystems, 17(11): 4725-4752.

Matthews, S., Wong, K., Shorttle, O., Edmonds, M. and Maclennan, J., 2021. Do Olivine Crystallization Temperatures Faithfully Record Mantle Temperature Variability? Geochemistry, Geophysics, Geosystems, 22(4).

Mollo, S., Putirka, K., Misiti, V., Soligo, M. and Scarlato, P., 2013. A new test for equilibrium based on clinopyroxene-melt pairs: Clues on the solidification temperatures of Etnean alkaline melts at post-eruptive conditions. Chemical Geology, 352: 92-100.

Neave, D.A. and Putirka, K.D., 2017. A new clinopyroxene-liquid barometer, and implications for magma storage pressures under Icelandic rift zones. American Mineralogist, 102(4): 777-794.

Putirka, K., 1999. Clinopyroxene + liquid equilibria to 100 kbar and 2450 K. Contributions to Mineralogy and Petrology, 135(2): 151-163.

Putirka, K.D., 2008. Thermometers and Barometers for Volcanic Systems. Reviews in Mineralogy and Geochemistry, 69(1): 61-120.

Rhodes, J., Dungan, M., Blanchard, D. and Long, P., 1979. Magma mixing at mid-ocean ridges: Evidence from basalts drilled near 22° N on the Mid-Atlantic Ridge. Tectonophysics, 55.

Spice, H.E., Fitton, J.G. and Kirstein, L.A., 2016. Temperature fluctuation of the Iceland mantle plume through time. Geochemistry, Geophysics, Geosystems, 17(2): 243-254.

Ubide, T., Mollo, S., Zhao, J., Nazzari, M. and Scarlato, P., 2019. Sector-zoned clinopyroxene as a recorder of magma history, eruption triggers, and ascent rates. Geochimica et Cosmochimica Acta, 251:

265-283.
Weit, A. et al., 2017. The magmatic system beneath the Tristan da Cunha Island: Insights from thermobarometry, melting models and geophysics. Tectonophysics, 716: 64-76.
Wieser, P. et al., 2022. Thermobar: An open-source Python3 tool for thermobarometry and hygrometry. Volcanica, 5(2): 349-384.
Wieser, P.E. et al., 2023. Barometers Behaving Badly I: Assessing the Influence of Analytical and Experimental Uncertainty on Clinopyroxene Thermobarometry Calculations at Crustal Conditions. Journal of Petrology, 64(2): egac126.
Wieser, P.E., Gleeson, M.L.M., Matthews, S., DeVitre, C. and Gazel, E., 2024. Determining the pressure-temperature-composition (P-T-X) conditions of magma storage. Treatise on Geochemistry (Third Edition).
Zhang, Y. et al., 2023. An extended calibration of the olivine–spinel aluminum exchange thermometer: Application to the melting conditions and mantle lithologies of large igneous provinces. Journal of Petrology: egad077.